THE SCUBA LEGACY CATALOGUES: SUBMILLIMETER-CONTINUUM OBJECTS DETECTED BY SCUBA

JAMES DI FRANCESCO,[1,2] DOUG JOHNSTONE,[1,2] HELEN KIRK,[1,2] TODD MACKENZIE,[3] AND ELIZABETH LEDWOSINSKA[4]

ABSTRACT

We present the SCUBA Legacy Catalogues, two comprehensive sets of continuum maps (and catalogs) using data at 850 and 450 μm of the various astronomical objects obtained with the Submillimetre Common User Bolometer Array (SCUBA). The Fundamental Map Data Set contains data only where superior atmospheric opacity calibration data were available. The Extended Map Data Set contains data regardless of the quality of the opacity calibration. Each data set contains $1.2° \times 1.2°$ maps at locations where data existed in the JCMT archive, imaged using the matrix inversion method. The Fundamental Data Set is composed of 1423 maps at 850 μm and 1357 maps at 450 μm. The Extended Data Set is composed of 1547 maps at 850 μm. Neither data set includes high sensitivity, single-chop SCUBA maps of "cosmological fields" nor solar system objects. Each data set was used to determine a respective object catalogue, consisting of objects identified within the respective 850 μm maps using an automated identification algorithm. The Fundamental and Extended Map Object Catalogues contain 5061 and 6118 objects, respectively. Objects are named based on their respective J2000.0 position of peak 850 μm intensity. The catalogues provide for each object the respective maximum 850 μm intensity, estimates of total 850 μm flux and size, and tentative identifications from the SIMBAD Database. Where possible, the catalogues also provide for each object its maximum 450 μm intensity and total 450 μm flux and flux ratios.

Subject headings: atlases — catalogs — submillimeter — techniques: image processing

Online material: machine-readable tables

1. INTRODUCTION

In 1996, the Submillimetre Common User Bolometer Array (SCUBA) was mounted on the 15 m diameter James Clerk Maxwell Telescope (JCMT)[5] near the summit of Mauna Kea. Since its commissioning, SCUBA allowed sensitive, widefield imaging of the submillimeter sky using the world's largest submillimeter telescope, itself located at one of the world's best submillimeter observing sites. During its lifetime, SCUBA was used extensively by astronomers from the three JCMT partner countries (the UK, Canada, and the Netherlands) and Hawaii, but also by many astronomers from other countries. SCUBA operated for almost 9 years; in early 2005, it was removed from the JCMT after cryogenics and gas handling system failures. A large part of the decision to remove SCUBA, rather than repair it, was that a powerful successor instrument, SCUBA-2 (see Holland et al. 2006) will be installed on the JCMT in early 2008.

Throughout its productive lifetime, SCUBA was used to probe submillimeter-continuum emission from a host of various astrophysical phenomena across the sky observable from Mauna Kea, from objects within the solar system to distant galaxies at high redshift. SCUBA data were made available to observers of approved projects immediately after their acquisition and were subject to a proprietary period of 1 year after the end of the semester of observation. After this period, however, the data were archived

at the Canadian Astronomy Data Centre (CADC)[6] and made available to the public. (Students working on dissertations with JCMT data could have this period extended.) SCUBA data are stored raw at the CADC, although preview images (made with a simple reduction) are available for individual files, allowing quick appraisals for data quality or source detection. Over ~9 years, however, many objects were observed over several epochs by different observers and the data spread over several projects and files. Submillimeter-continuum maps could be significantly improved by optimally combining these separate data prior to forming final images.

In this paper, we describe a project to image almost all SCUBA data sets, using raw data from all epochs, to provide an archive of images at 850 and 450 μm that were reduced consistently by a single method (i.e., the "matrix inversion" method described by Johnstone et al. 2000a) and using the most current calibrations (i.e., extinction corrections and flux conversion factors [FCFs]). The images are themselves available for download at the CADC as FITS files (see § 8 for access instructions). We provide here, however, examples of some of the spectacular maps produced by SCUBA over its lifetime. In addition, we present catalogs drawn from these images of submillimeter-continuum objects mapped by SCUBA, found using an automated object identification program (based on the CLUMPFIND algorithm of Williams et al. 1994). No catalog of objects at submillimeter wavelengths akin to the extremely useful catalogs at near- to far-infrared wavelengths (e.g., the *Catalog of Infrared Observations* by Gezari et al. [1984, 1988] or the IRAS Catalogues [see Beichman et al. 1988]) currently exists. Since the maps produced here are derived from previous SCUBA data, only a relatively limited amount of sky is covered; the resulting catalogs are not "all sky." Many well-known objects and regions were mapped extensively with

[1] National Research Council of Canada, Herzberg Institute of Astrophysics, 5071 West Saanich Road, Victoria, BC V9E 2E7, Canada.

[2] Department of Physics and Astronomy, University of Victoria, Elliot Building, 3800 Finnerty Road, Victoria, BC V8P 5C2, Canada.

[3] Department of Physics, University of Prince Edward Island, 550 University Avenue, Charlottetown, PE C1A 4P3, Canada.

[4] Department of Physics, McGill University, Ernest Rutherford Physics Building, 3600 rue University, Montréal, QC H3A 2T8, Canada.

[5] The James Clerk Maxwell Telescope is operated by the Joint Astronomy Centre on behalf of the Particle Physics and Astronomy Research Council of the United Kingdom, the Netherlands Association for Scientific Research, and the National Research Council of Canada.

[6] The Canadian Astronomical Data Centre is operated at the Dominion Astrophysical Observatory for the National Research Council of Canada.

SCUBA, however. The catalogs provide a context for understanding the voluminous maps that will be produced by SCUBA-2 and are themselves a useful planning tool for future observations with new submillimeter and millimeter interferometers (e.g., SMA, CARMA, ALMA). The catalogs discussed here will be linked with other catalogs at the CADC.

In what follows, we describe SCUBA in § 2, our uniform reduction procedure in § 3, and a global description of the resulting maps in § 4. In addition, we describe our object identification algorithm in § 5, the SCUBA map object catalogues and their contents in § 6, and several example regions in § 7. A description of the available data products is provided in § 8. Finally, a summary is provided in § 9.

2. A BRIEF DESCRIPTION OF SCUBA

A full description of the instrumental characteristics of SCUBA was made by Holland et al. (1999). Here we describe the instrument in brief to provide the context for the maps and catalogs. SCUBA was built by the Royal Observatory Edinburgh for the James Clerk Maxwell Telescope. It consisted of 128 bolometers arranged into two hexagonally packed arrays, the Long-Wave (LW) array with 37 bolometers and the Short-Wave (SW) array with 91 bolometers, as well as three additional bolometers surrounding the LW array. Simultaneous illumination of the LW and SW arrays was achieved by dichroic beam splitting, allowing for sampling at two wavelengths across 2.3′ of sky in a single pointing. SCUBA's original filter set allowed for simultaneous observations in the LW and SW arrays either at 750 and 350 μm or at 850 and 450 μm. (The 3 additional bolometers surrounding the LW array allowed for single-pixel observations at 1100, 1300, and 2000 μm.) Most SCUBA observations, however, were made at 850 and 450 μm, in part because the filter wheel became stuck at this pair in 1997. All SCUBA bolometers were cooled to <1 K, allowing sky background noise sensitivity levels to be achieved. Subtraction of the sky was enabled by sampling off-target locations repeatedly during observations using the chopping subreflector of the JCMT. Note that chopping has a profound effect on SCUBA data, as emission on angular scales larger than the chop throw effectively is spatially filtered out of the resulting maps. At 850 and 450 μm, the resolutions of SCUBA data were represented to first order by Gaussians of $\sim$14″ and $\sim$9″ FWHM, respectively, although significant "error beams" were also present, especially at 450 μm (Hogerheijde & Sandell 2000; see also § 3). These "error beams" must be taken into account when determining fluxes (see §§ 4 and 5).

SCUBA was used to observe the submillimeter sky in three specific modes. As mentioned above, at all times the contaminating sky emission was removed via chopping with the subreflector. The first was a "photometry" mode used for maximum sensitivity at the location of the central bolometer, i.e., the telescope effectively stared at a fixed location to maximize received signal from a single target. The second was a "jiggle" mode, used to make Nyquist-sampled maps across the SCUBA field of view, i.e., the telescope was moved in a fixed pattern to positions offset from each other by fractions of the beam to fill in spaces between the individual bolometers. The third was a "scan" mode used to make larger scale maps at the expense of sensitivity at any given position, i.e., the telescope was slewed over relatively large distances (typically 10′), producing strips along the sky which could be stitched together. By carefully choosing the angle with respect to the bolometer array that the telescope moved, the spacing between measurements Nyquist-sampled the sky. All three modes allowed differential continuum intensities to be measured. Polarized continuum emission, however, could also be observed across

the arrays by using a rotating quartz half-wave plate, but only in photometry or jiggle mode.

3. MAP DATA PROCESSING

Since the goal of this project was to make maps and then catalog objects therein, all raw jiggle and scan data from SCUBA available in the JCMT archive were downloaded from the CADC in 2006 May. (Photometry and polarimetry data were ignored.) In addition, SCUBA data taken at wavelengths other than 850 or 450 μm were not retrieved. The downloaded data consisted of 35,455 "SCUBA Data Files" describing for each bolometer the time of measurement, the location observed on the sky, and the measured voltage difference between that position and a specified off-position. The 850 and 450 μm map data retrieved should have comprised all those normally available to the public at these wavelengths, since the instrument had ceased operations >1 yr earlier. In total size, the raw data were only 78.7 GB.

Further culling of the raw data ensemble was necessary. Data of objects in the solar system (e.g., planets, asteroids, comets) were removed, since these objects have time-varying positions, angular sizes, and brightnesses. Such files were located by visually inspecting the list of unique "target names" attached to each. (Those interested in SCUBA maps of solar system objects at particular epochs can download them directly from the CADC.) In addition, a small number of data attached to peculiar target names (e.g., "whatever" or "reflector") were also removed from the ensemble. Only 28,534 SCUBA data files remained after culling solar system and peculiar objects. In size, these culled data were 69.9 GB. Figure 1 shows the locations on the sky of all the SCUBA maps described in this paper; well-sampled areas such as the Galactic plane and nearby molecular clouds like Orion and Ophiuchus are clearly visible.

Atmospheric attenuation dominates the raw voltage difference measurements and the effect of such attenuation must be calibrated out in the data to obtain proper voltage levels for observed sources. The SCUBA data were calibrated separately at 850 and 450 μm using the standard ORAC-DR program, part of the STARLINK package (Economou et al. 1999). Overall, 99.98% of the raw files could be calibrated with ORAC-DR without error, and those remaining were discarded. The baseline atmospheric opacity data for SCUBA calibration were obtained from a combination of skydips made with SCUBA itself and contemporaneous tipping scans made by a dedicated 225 GHz radiometer (the "CSO 225 GHz Dipper") located at the nearby Caltech Submillimeter Observatory (CSO).[7] See Archibald et al. (2002) and Weferling (2005) for wide discussions of SCUBA calibration and how these data were tabulated for use in reducing SCUBA observations. Superior atmospheric correction uses a low-order polynomial fit in time to a combination of the two opacity determinations but was available for only 77.77% of the SCUBA map data set. For the rest of the data, the CSO 225 GHz Dipper measurement, stored in the observation header, could be used to estimate the sky opacity at 450 and 850 μm, although with much larger uncertainty in the conversion.

Given the importance of proper opacity correction, 850 and 450 μm maps were first made with only the $\sim$78% of data where superior atmospheric correction data were available. These maps compose the "Fundamental Map Data Set" and these should be referred to when interested in the most accurate fluxes. To expand the scope of the maps, additional 850 μm maps were made using *all* available data. These latter data compose the "Extended Map Data Set," and these should be referred to when interested

---

[7] For the first half of 2003 the NRAO dipper was used as a substitute for the CSO 225 GHz Dipper due to complications with the CSO instrument.
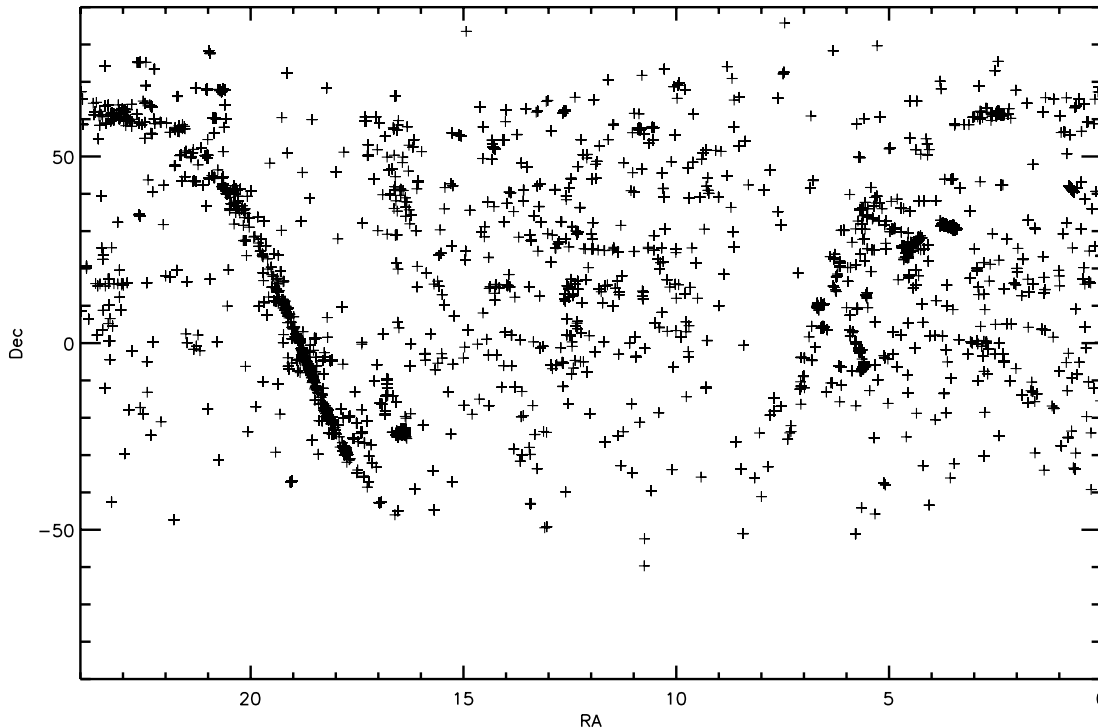
Fig. 1.—Distribution of SCUBA mapping locations across the sky, excluding observations of solar system objects (see text), where each J2000.0 position observed is denoted by a cross. Some crosses are darker than others, because they are the superposition of several observations made in close proximity.

in the widest areal coverage. The Extended Map Data Set does not include 450 μm maps because of the greater importance of accurate opacity calibration at shorter submillimeter wavelengths. In what follows, we treat the Fundamental and Extended Map Data Sets equally, and provide catalogs derived from each.

With a 9 year lifetime, the weather conditions when SCUBA was used varied significantly, of course. Figure 2 shows histograms of opacity values at 850 and 450 μm from data within the Fundamental Data Set, demonstrating the spread of opacity values when SCUBA observed.

As well as calibrating the sky opacity corrections, the conversion between voltage difference and flux must be determined. Jenness et al. (2002) showed that over extended periods (typically semesters) during which no significant changes to the telescope and electronics were performed, the FCF was essentially constant with an uncertainty of approximately 10% and 25% at 850 and 450 μm, respectively. Most of the uncertainty is caused by changes in the telescope surface, due to temperature and gravity deformations, producing changes in the beam profile. The corresponding FCF values are tabulated and available for use in data reduction.

To facilitate the creation of useful maps, the sky was divided into square degree regions (actually each was $1.2° \times 1.2°$ in extent, with $0.1°$ overlap with neighboring fields) using Galactic coordinates and the individual observations composing the data sets were sorted into bins corresponding to these regions. The maps themselves, however, are stored in J2000.0 equatorial coordinates.

Maps of each square degree region were then made individually using the mapfits program using the respectively sorted calibrated map data as inputs. This program is based on the matrix inversion scheme described by Johnstone et al. (2000a), which produces better images from chopped data than techniques such as the Fourier deconvolution (e.g., Emerson et al. 1979; Emerson 1995). In addition, the matrix inversion method allows the combination of data taken with different observing setups, such as jiggle and scan observations. Furthermore, data from specific bo-

lometers are weighted appropriately by their respective associated noise levels. Finally, the image fidelity and dynamic ranges achieved by the matrix inversion method are good; see Johnstone et al. (2000a) for examples where sources of known brightness are artificially included into maps.

Previously published examples of SCUBA maps made via matrix inversion include those of molecular clouds in Ophiuchus (Johnstone et al. 2000b, 2004), Perseus (Kirk et al. 2006), and Orion (Johnstone et al. 2001, 2006; Johnstone & Bally 2006). In addition, L1551 in Taurus (Moriarty-Schieven et al. 2006) explicitly demonstrates the power of the mapfits algorithm for bringing together heterogeneous SCUBA observations.

Pixel sizes for the 850 and 450 μm maps were defined at $6''$ and $3''$, respectively. For each square degree region, 3 maps were created at each wavelength: an emission map with sky intensity pixels in Jy beam^{-1}, an error map with standard deviation values at each pixel, and a coverage map with each pixel containing the number of times its position was observed with SCUBA. The resulting maps are projected onto a tangent plane associated with the center of each square degree field.

A small amount of data had problems that required their respective files to be excised from the various square degree regions. These problems included: (1) data listed as "not a number" (NaN), (2) data that caused segmentation faults when running mapfits, (3) data associated with a "wrong number of bolometers," and (4) data with pixels of extremely high ("infinite") noise. After discarding these files, the corresponding square degree maps were remade using mapfits.

Each square degree map was further processed to remove artifacts. First, noisy edges in each map were clipped. Since such edges resulted from there being relatively few observations at the associated pixels, the coverage maps were used to find pixels in the data maps at locations with less than 15 observations, and these were clipped. (The number maps were first smoothed with a Gaussian kernel of $\sigma_G = 7$ pixels to minimize pixel-to-pixel
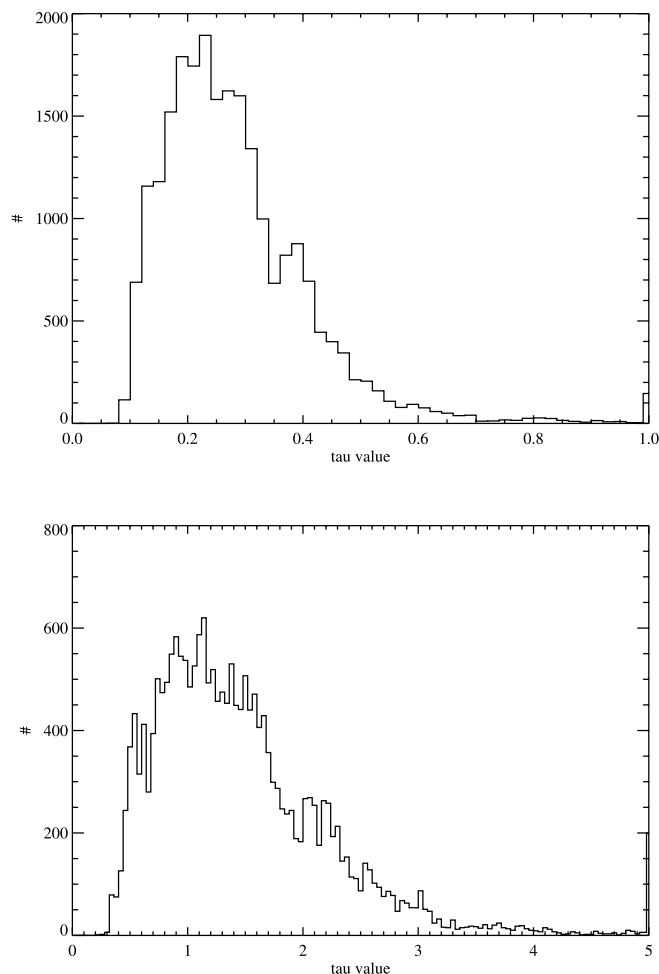
Fig. 2.—Histograms of optical depth ("tau") values measured at 850 μm (*top*) and 450 μm (*bottom*) for data within the Fundamental Data Set. Note that the histograms show only the majority of measured values, and the bins at the extreme right contain the totals at values greater than or equal to the respective extremes.

variations. Note that the square degree maps may contain data of different sensitivities due to differing integration times or opacity conditions during separate observations of nearby targets.) Second, the data maps themselves were smoothed with a Gaussian kernel of $\sigma_G = 1$ pixel to minimize pixel-to-pixel noise; in effect, this increased the expected resolutions of the maps to $\sim$19$''$ FWHM at 850 μm and $\sim$11$''$ at 450 μm (but see § 4). Third, the data maps were flattened to remove the large spatial scale variations that occurred due to imperfect cancellation of sky signal through chopping. Flattening was performed by first filtering and smoothing the original clipped data map with a Gaussian of large kernel size, and then subtracting this map from the smoothed and clipped data map. To prevent excessive bowling around bright sources, pixels with values >5 times the median noise in the original clipped map were replaced by pixels with values equal to 5 times the median noise. Filtering was effective in reducing common artifacts where bright emission is surrounded by a bowl of negative pixels. For smoothing, the filtered data map was smoothed with a Gaussian kernel of $\sigma_G = 20$ pixels for the 850 μm data and 40 pixels for the 450 μm data. (After subtraction, edge pixels that had been previously clipped were reclipped.)

To improve flux calibration, processed maps that contained three pointlike objects, HL Tau, CRL 618 (PN G166.4−06.5), and CRL 2688 (the Egg Nebula), were examined. The 850 and 450 μm continuum maximum intensities and total fluxes of these three objects were well determined by JCMT staff for better calibration of SCUBA data. The comparison between the expected maximum intensities and those found in the processed maps at both wavelengths yielded correction factors that were applied to all 850 and 450 μm processed maps. Table 1 lists the expected maximum intensities of all three objects at both wavelengths, and the maximum intensities and total fluxes found in the processed maps after the respective correction was made. Small differences between the expected and "observed" maximum intensities and fluxes still persist, but these are likely due to small variations in intrinsic source structure, noncentering of the object maximum intensities in a single pixel, and variations of observing conditions between objects. As described in § 4, the absolute flux uncertainties of SCUBA data have been historically $\sim$20% at 850 μm and $\sim$50% at 450 μm.

Each flux-corrected and processed square degree map was visually inspected for quality. In some maps containing jiggle data, periodic structures (i.e., ripples) were seen. Such ripples can be introduced to maps when data obtained with nonstandard setups or during times of instrumental failure are included. (Data were not placed into the JCMT Archive with a quality flag.) In addition, such ripples may arise when jiggle data are obtained with only one chop throw and angle, which precludes the kind of interconnectivity between data points that benefits maps made by matrix inversion. Such data are susceptible to amplification of the chop signal during reconstruction. This effect typically does not occur over the spatial scale of a single jiggle map, but when many jiggle maps are combined to make a larger map, each with a single chop throw and angle, the opportunity increases for amplification due to degeneracy in reconstruction. Unfortunately, many fields that were observed for high sensitivity to detect faint high-redshift galaxies, including the Hubble Deep Field, the Groth Strip, and the SHADES fields (the Subaru/*XMM-Newton* Deep Field and the Lockman Hole) were observed with a single chop throw and angle, and we were unable to produce satisfactory maps of these regions. All square degree maps entirely containing such periodic structure, including these "cosmological" fields, were removed from the ensembles after visual inspection. (Those interested in such fields should look at the respective papers where the data have been very carefully processed, e.g., see Coppin et al. [2006] for the SHADES fields.) Square degree maps containing regions of reasonable quality but localized regions with periodic structure (e.g., one with good scan or jiggle data in some locations but rippled jiggle data in other locations) were retained, however. Objects found from these maps at locations of periodic structure were removed from catalogs after further visual inspection (see § 4).

4. MAP RESULTS

In the Fundamental Map Data Set, 1423 square degree maps contain SCUBA map data at 850 μm and 1357 square degree maps contain SCUBA map data at 450 μm. (Note that 214 of the Fundamental 850 μm maps and 213 of the Fundamental 450 μm maps contain data only in the outer 0.1° of each 1.2$^\circ \times$ 1.2° field; these locations are also found within the central square degree in other maps of adjacent fields.) In total, the 850 μm Fundamental maps contain $\sim$7.06 $\times$ 10^6 pixels for a total areal coverage of 19.6 deg^2. The 450 μm Fundamental maps contain a total of 23.6 $\times$ 10^6 pixels for a total areal coverage of 16.4 deg^2. The smaller areal coverage of the 450 μm maps reflects the fact that at times only the 850 μm data from the telescope was stored during observations. (Often this occurred during fast scans, where the telescope was slewed at an accelerated rate, and any 450 μm observations were significantly undersampled.) In the Extended Map

TABLE 1
Expected vs. Observed Fluxes of Pointlike Calibrators

Name (1)	850 μm			450 μm		
	Expected Peak (Jy beam^{-1}) (2)	Observed Peak (Jy beam^{-1}) (3)	Observed Flux (Jy) (4)	Expected Peak (Jy beam^{-1}) (5)	Observed Peak (Jy beam^{-1}) (6)	Observed Flux (Jy) (7)
HL Tau	2.35 ± 0.08	2.4	2.1[a]/1.9[b]	9.4 ± 1.3	12	8.6
CRL 618	4.6 ± 0.2	4.4	5.0[a]/4.1[b]	10.9 ± 0.9	8.2	8.9
CRL 2688	5.9 ± 0.2	5.8	5.2[a]/5.1[b]	22.0 ± 2.7	24	19

[a] Flux calculated from full area of object.
[b] Flux calculated from area within 90 mJy beam^{-1} contour.

Data Set, 1547 square degree maps contain SCUBA map data at 850 μm. (Note that 234 of these maps contain data only in the outer $0.1°$ of each $1.2° \times 1.2°$ field.) These maps contain a total of 10.6×10^6 pixels for a total areal coverage of 29.3 deg^2, i.e., $\sim 50\%$ larger than in the Fundamental Map Data Set at 850 μm.

Figures 3–6 show examples of maps assembled from the data processed in this effort, for low-mass star-forming regions, high-mass star-forming regions, nearby galaxies, and debris disks, respectively. These data, as with all data described here, are available for public use at the CADC.

Figure 7 shows one-dimensional profiles of the JCMT beams at 850 μm (*bottom*) and 450 μm (*top*), clipped to highlight the relative magnitude of the departure from Gaussian profiles, i.e., the error beams. These profiles were obtained from slices across Fundamental Data Set data of the pointlike source CRL 618 (PN G166.4−06.5). As a common SCUBA calibrator, CRL 618 was observed numerous times over SCUBA's lifetime, and the data shown in Figure 7 are composites of all the map data of CRL 618 in the archive with proper flux calibration. Figures 7a and 7b show the one-dimensional profiles at 450 and 850 μm, respectively, that were obtained from maps of CRL 618 made with $1''$ pixels. Figures 7c and 7d show one-dimensional profiles of the same object again at 450 and 850 μm, respectively, but obtained from maps made with $3''$ and $6''$ pixels, as in both data sets. In each case, the beams show clear non-Gaussian features, but can be effectively represented by a sum of two Gaussians, a narrow "primary" beam of FWHM approximately that of the expected resolution of the telescope at a given wavelength and smoothing and a wide "error beam" of $40''$ FWHM independent of wavelength. For the $1''$ maps, the 450 μm beam contains a primary beam of $8.5''$ FWHM and 0.90 relative peak, and the 850 μm beam contains a primary beam of $13.5''$ FWHM and 0.96 relative peak. The values we obtain are consistent with those obtained by Hogerheijde & Sandell (2000), who used data of Uranus from 1997 September, although they included a third very wide low-amplitude Gaussian in their beam models at each wavelength. For the $6''$ maps, the 450 μm beam contains a primary beam of $11''$ FWHM and 0.88 relative peak, and the 850 μm beam contains a primary beam of $19.5''$ FWHM and 0.88 relative peak. (At both wavelengths, the secondary beam has $40''$ FWHM and 0.12 relative peak.) These larger values are due to the effective smoothing that comes with using larger pixels but are also due to the additional smoothing by $\sigma_G = 1$ pixel applied to each map to reduce pixel-to-pixel noise. The effective FWHMs of the beams in each data set are $17.3''$ at 450 μm and $22.9''$ at 850 μm. These beam values are used in the computation of the observed fluxes below (see § 6).

Since the maps were taken over a variety of different weather conditions and methods, there is no common noise level representative of the entire data set. Some maps are also composites of several different observing runs, and so the noise level within any given map may not be uniform. Figure 8 presents a histogram showing the distributions of 1 σ rms across pixels in the Fundamental and Extended maps. The 850 μm distributions have Poissonian characters, i.e., peaks at small values (~ 40 mJy beam^{-1}) and long tails to large values. The median values of the rms at 850 μm are 71.0 and 76.2 mJy beam^{-1} for the Fundamental and Extended maps, respectively. The 450 μm distribution has two peaks, however, a narrow one at ~ 50 mJy beam^{-1} and a broad one at ~ 380 mJy beam^{-1}. The median value of the rms at 450 μm is 820 mJy beam^{-1}. Note that the pixels oversample the beam at both wavelengths, so the noise at a given pixel is larger than the noise within a fixed beam. In addition, for object identification (see § 5), we use the median noise per pixel associated with the individual objects under investigation and not the median noise values of each entire square degree map.

Absolute flux uncertainties in the SCUBA maps were dominated by fluctuations of opacity above the telescope during observations and calibration. Typical absolute flux uncertainties of SCUBA maps have been historically $\sim 20\%$ at 850 μm and $\sim 50\%$ at 450 μm (Matthews 1993), reflecting almost equal contributions from flux calibration and beam-shape uncertainty. We adopt these uncertainties for the catalogues in this paper. As seen in Table 1, the maximum intensities and fluxes of the three pointlike calibrators HL Tau, CRL 618 (PN G166.4−06.5), and CRL 2688 (the Egg Nebula) have values within these uncertainties. For further discussion of the uncertainties in object fluxes, see § 7.2.

Each map was made using positional data that accompanied the respective SCUBA data files. Pointing accuracy for SCUBA was typically $\sim 3''$ and tracking accuracy was typically $\sim 1.5''$ (H. Matthews 2006, private communication). Larger pointing offsets did occur during observations occasionally. For example, SCUBA data of the young stellar cluster NGC 1333 required positional corrections of $\sim 6''$ to line up peaks with data from other wavelengths (Sandell & Knee 2001). Given the lack of common positional references at other wavelengths across all map areas, however, we have performed no positional fine-tuning on the maps. For further discussion of the uncertainties in positions, see § 7.3.

Despite the care given to improving the maps here, they still may retain defects. For example, some bright objects can still be surrounded by negative "bowls" that are obviously artificial. In addition, map edges may still contain extended (positive or negative) artifacts from proper removal of sky emission that remain despite flattening the map. Higher accuracy determination of fluxes and source morphologies requires significant user interaction when mapmaking. The maps presented here should not be used when the highest precision is required, rather for such regions extreme consideration of the calibrations, etc., should be performed. We expected, however, that the vast majority of information
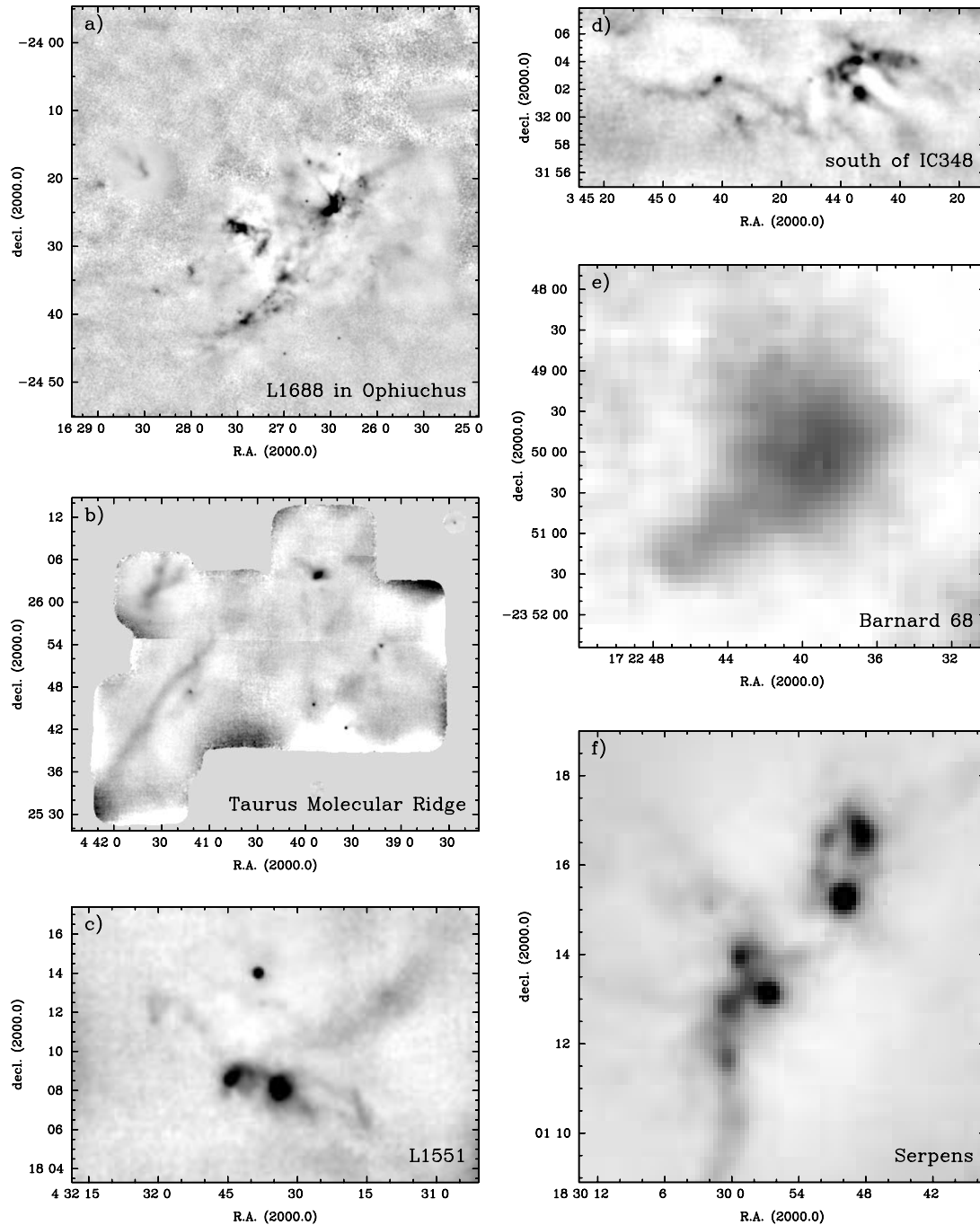
Fig. 3.—Examples of SCUBA 850 μm observations of low-mass star-forming regions from the Extended Data Set. Gray-scale ranges are chosen to bring out low-level features in the maps. (*a*) L1688 cluster region in the central part of the Ophiuchus molecular cloud with gray scale ranging from −0.2 to 1.1 Jy beam^{-1}. (*b*) Central part of the Taurus molecular cloud with gray scale ranging from −0.1 to 0.6 Jy beam^{-1}. (*c*) L1551 cloud, south of the Taurus molecular cloud with gray scale ranging from −0.1 to 0.6 Jy beam^{-1}. (*d*) Region of young star formation south of IC 348 in the Perseus molecular cloud with gray scale ranging from −0.1 to 0.6 Jy beam^{-1}. (*e*) Isolated starless core Barnard 68 with gray scale ranging from −0.04 to 0.21 Jy beam^{-1}. (*f*) Bright, clustered protostellar sources of the Serpens molecular cloud with gray scale ranging from −0.6 to 3.2 Jy beam^{-1}.

contained in the archival SCUBA data has been efficiently presented in these maps.

5. OBJECT IDENTIFICATION

We describe here the methods used to extract information about the objects detected in the 850 μm SCUBA maps. We did not use the 450 μm maps to define objects given the lower accuracy of its flux calibration and the smaller number of 450 μm maps. The identification of objects from submillimeter-continuum emission is tricky, because the emission itself can range in maps

from being quite compact (e.g., on the order of the beam size) to quite extended (e.g., beyond the chop throw angular distance, although on these scales it becomes attenuated by the observing techniques). In addition, such objects can be themselves either bright or dim and can be arranged in compact or diffuse associations.

To identify objects, we applied to every 850 μm square degree map the two-dimensional CLUMPFIND algorithm, developed first for three-dimensional cubes of molecular line data by Williams et al. (1994) and adapted for use on SCUBA continuum maps. CLUMPFIND works by following isointensity contours within
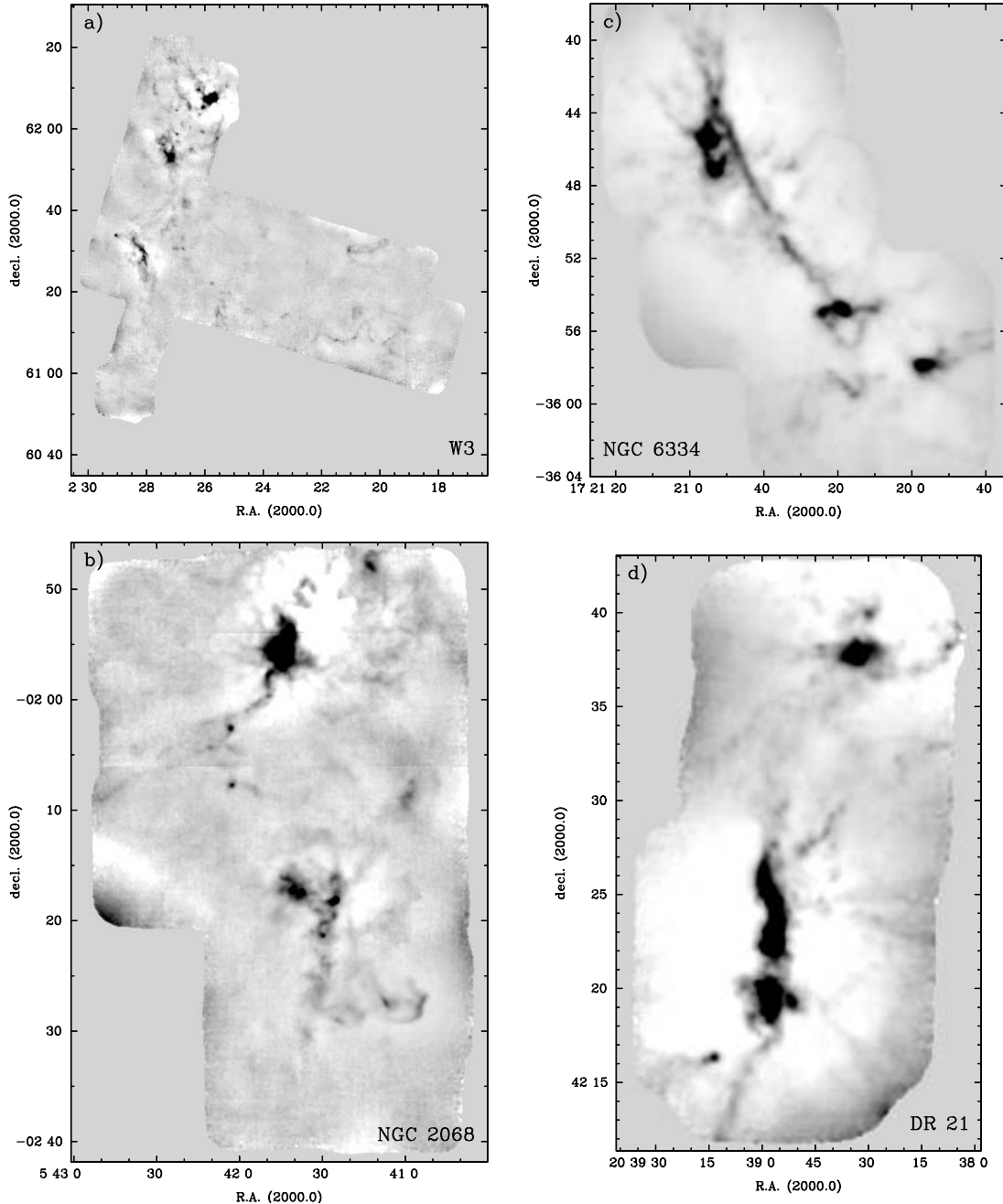
FIG. 4.—Examples of SCUBA 850 μm observations of high-mass star-forming regions from the Extended Data Set. Gray-scale ranges are chosen to bring out low-level features in the maps. (*a*) Inner part of the W3 molecular cloud with gray scale ranging from -0.2 to 1.1 Jy beam^{-1}. (*b*) NGC 2068 region of the Orion B molecular cloud (including the Horsehead Nebula) with gray scale ranging from -0.2 to 1.1 Jy beam^{-1}. (*c*) NGC 6334 filament with gray scale ranging from -2.0 to 11 Jy beam^{-1}. (*d*) DR 21 region with gray scale ranging from -0.4 to 2.1 Jy beam^{-1}.

maps, defining objects by emission within a closed contour either 2 σ below a predefined sensitivity limit (e.g., 5 σ) or higher if a neighboring object is encountered at a higher contour level. Since objects are defined only in terms of closed contours, CLUMPFIND does not presuppose a particular source structure for its identifications, e.g., Gaussians. Since the noise level will significantly vary across any map comprising observations of separate objects at different epochs, 3 times the minimum noise levels of a given map were used first to define objects. For each object candidate, CLUMPFIND returns its peak intensity and the position of peak intensity, as well as its total flux density and size based on the number of pixels within the closed contour of definition. CLUMPFIND also produces an "object map" that identifies pixels with specific objects. By using a minimum noise threshold in every map, the algorithm was driven in a first pass to include as many object candidates as possible; many of these had maximum intensities not more than a few times their local median noise levels, however.

After initial identification, three criteria were applied to each object candidate to determine its reality as an astronomical source and improve the robustness of the object lists. First, objects were discarded if their peak pixel values were less than 3 times the median of the noise in the pixels that defined it. Second, objects were discarded if their sizes were less than the areal size of the effective beams (e.g., ≤ 8 pixels at 850 μm). Third, objects were removed if they were located near the edges of maps, where large-scale fluctuations tended to remain even after flattening. For scan
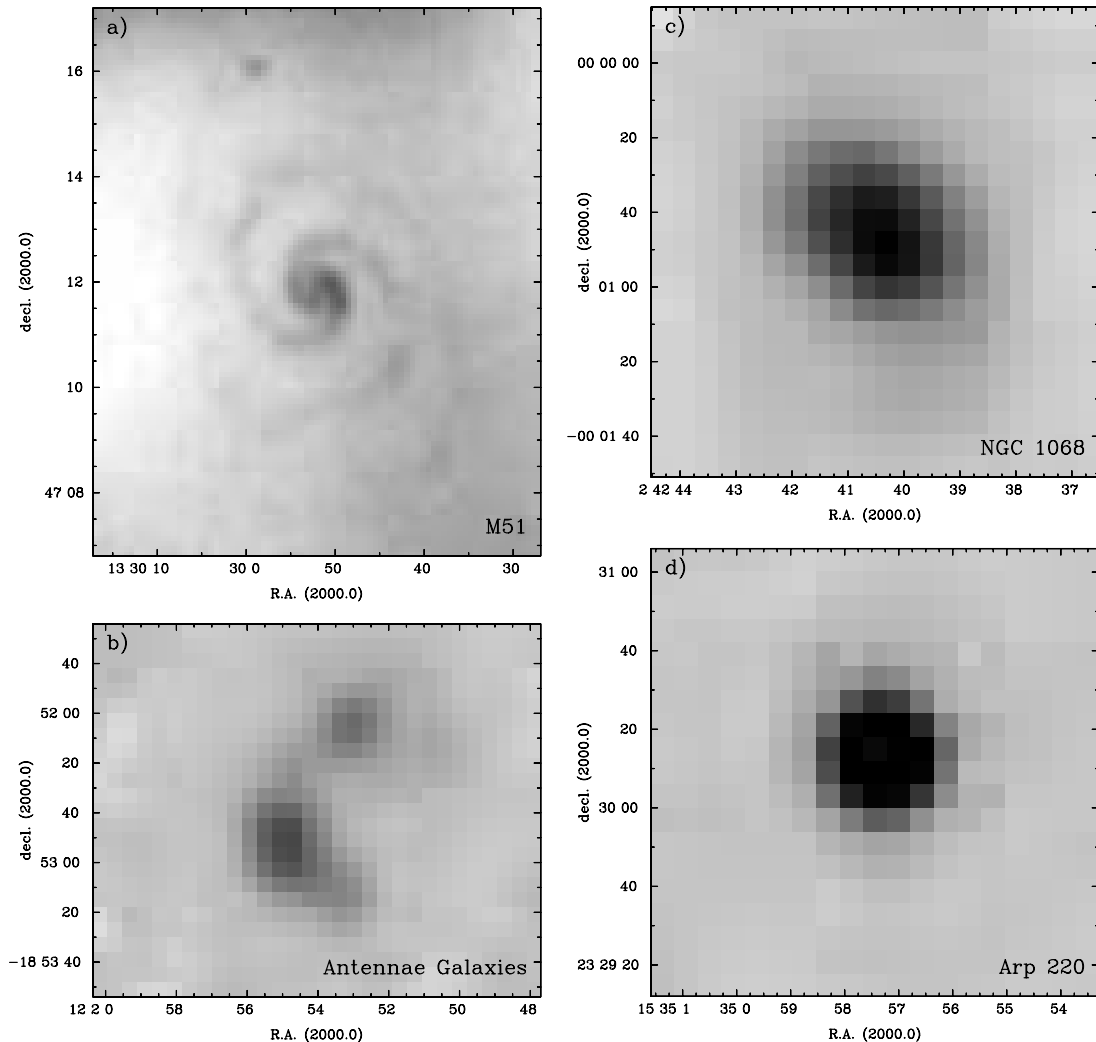
FIG. 5.—Examples of SCUBA 850 μm observations of nearby galaxies from the Extended Data Set. In all panels, the gray scale ranges from -0.1 to 0.32 Jy beam^{-1}. (*a*) Whirlpool Galaxy (M51). (*b*) Central part of the colliding Antennae galaxies (NGC 4038/4039). (*c*) Nearby galaxy NGC 1068. (*d*) Peculiar galaxy Arp 220.

maps, identified objects with peaks within 25 pixels along the cardinal directions to the map edges were discarded if they were adjacent to other sources that adjoined the map edge. For jiggle maps, no such removals were done, given their innately smaller sizes. Identified objects adjoining jiggle map edges, however, were identified as such (see § 6), since it is likely they have been incompletely sampled or characterized (if indeed such objects are real).

Note that since CLUMPFIND depends on the noise characteristics of a given map to define objects, the objects found in the Fundamental and Extended Map Data Sets may differ. For example, an extended object identified as single in one data set may be identified as multiple objects in the other data set. This dependence on noise is the reason why two object lists have been provided, rather than a single hybrid object list. As an example, Figure 9 illustrates differences between objects identified in L1688 of Ophiuchus in the Fundamental and Extended Data Sets.

CLUMPFIND is by no means the perfect method for identifying objects in SCUBA maps. It has, however, an attractive simplicity and generality that allowed it to be used on large map data sets (Johnstone et al. 2000b, etc.) Other methods used to identify objects in (sub-) millimeter continuum maps include various wavelet decomposition schemes (e.g., see Motte et al. 1998 or Knudsen

et al. 2006) or peak-finding algorithms related to CLEAN-style deconvolution (e.g., see Enoch et al. 2006 or Young et al. 2006). As described by Enoch et al., CLUMPFIND recovers well total flux densities in crowded regions of compact sources where blind aperture photometry is inappropriate. In addition, the CLUMPFIND algorithm does not unnecessarily divide up extended emission into multiple objects. CLUMPFIND, however, likely underestimates the total flux densities for isolated or faint sources, since significant source flux may reside below the predefined signal threshold limit. (See § 7.1 for further discussions about the limitations of this technique.)

6. THE CATALOGUES

In this section, we describe the catalogues based on the Fundamental and Extended Data Sets. Tables 2 and 3 list the Fundamental Map Object Catalogue (FMOC) and the Extended Map Object Catalogue (EMOC), respectively. The FMOC and EMOC contain objects identified at 850 μm from the Fundamental and Extended Map Data Sets, respectively (see § 4). Again, the Fundamental Map Data Set includes only the 77.77% of SCUBA map data for which proper opacity data from both skydips and the CSO radiometer were available, while the Extended Map Data Set includes all SCUBA map data deemed usable, i.e., data for which
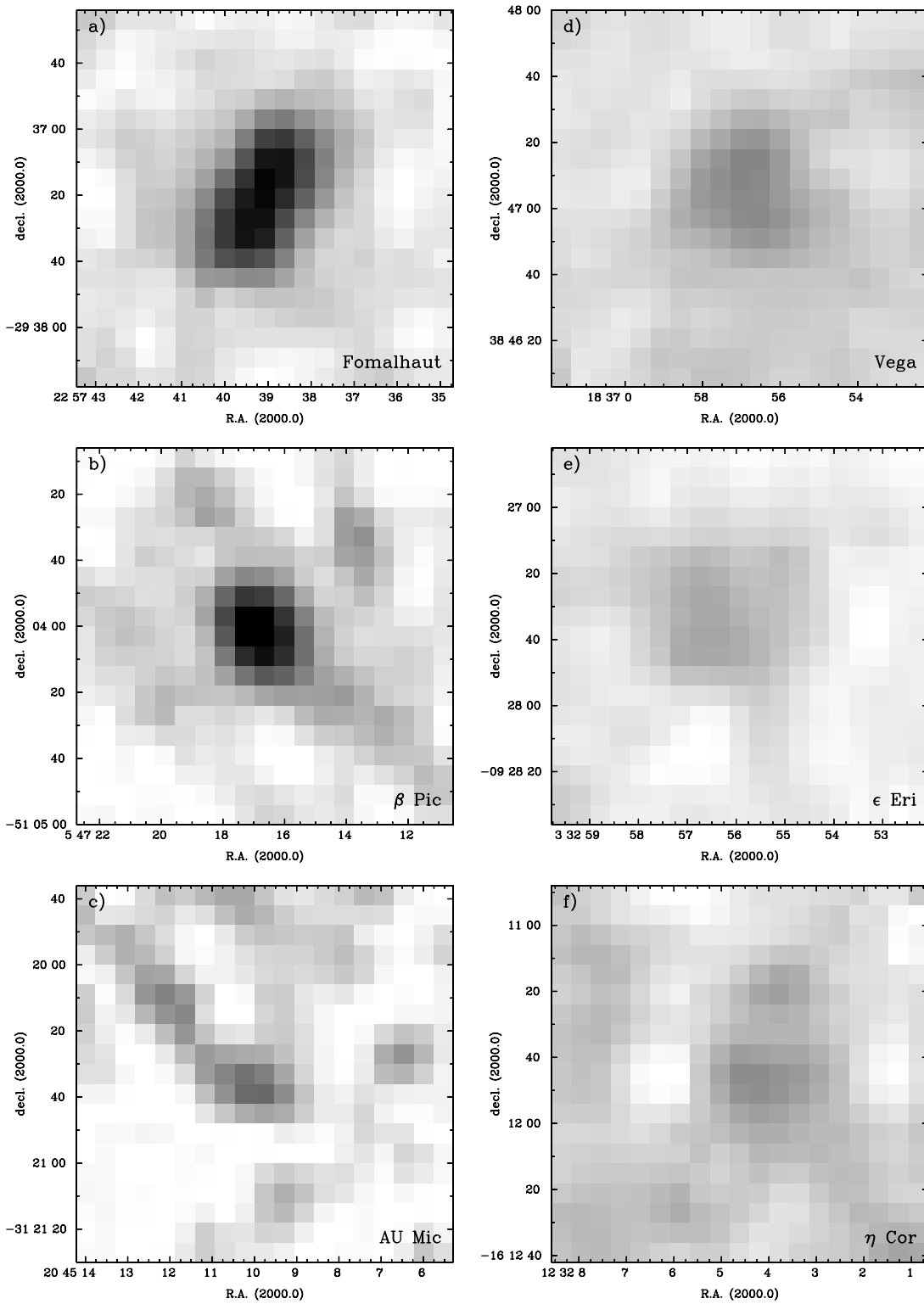
FIG. 6.—Examples of SCUBA 850 μm observations of debris disks around main-sequence stars. In all panels, the gray scale ranges from -0.006 to 0.04 Jy beam^{-1}. (*a*) α PsA (Fomalhaut). (*b*) β Pic. (*c*) AU Mic. (*d*) α Lyr (Vega). (*e*) ϵ Eri. (*f*) η Crv.

only radiometer data were stored in the header. (The Extended Map Data Set includes only maps at 850 μm, however.) In total, the FMOC contains 5061 objects, and the EMOC contains 6118 objects, 20.4% more than the FMOC.

The following description of the columns of Tables 2 and 3 applies to their electronic versions. Columns (4) and (15)–(26)

described below are not present in the print versions of Tables 2 and 3.

Column (1) lists the object name, based on the position of its pixel of maximum brightness at 850 μm in J2000.0 coordinates. The convention used is "JCMTSn_JHHMMSS.S $\pm$ DDMMSS," where "JCMTS" is short for JCMT/SCUBA and n is either "F" or

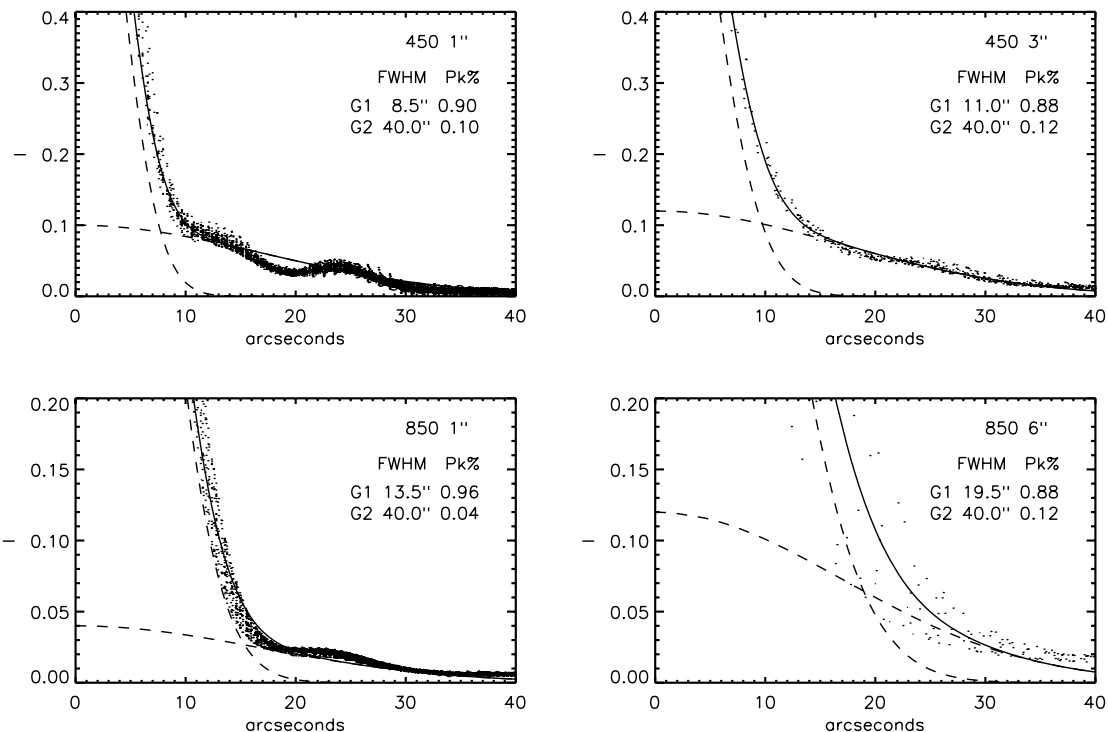Fig. 7.—Low-level structure in the JCMT beams at 450 μm (*top panels*) and at 850 μm (*bottom panels*), from numerous observations of the calibrator source CRL 618 (PN G166.4−06.5). In each plot, the dots show pixel values normalized to the peak intensity. Solid lines show Gaussian profiles fit to the profile by eye from the summation of the two other Gaussian profiles shown as dashed lines. *Left*: Images of CRL 618 made with 1″ pixels. *Right*: Fundamental Data Set images (i.e., 3″ pixels at 450 μm and 6″ pixels at 850 μm.)

"E" depending on whether the object is in the Fundamental or Extended Catalogues, respectively. In addition, "J" indicates that the following coordinates are in the J2000.0 epoch. HHMMSS.S denotes the hours, minutes, and seconds in right ascension and ±DDMMSS is the degrees, minutes, and seconds in declination of the pixel of maximum intensity. Columns (2) and (3) list respectively the Galactic coordinates[8] l and b for each object, based on the J2000.0 coordinates from column (1). Column (4) lists the name of the FITS file containing the 850 μm square degree map from which the object was identified.

Columns (5)–(9) list some 850 μm characteristics for each object. Column (5) lists the object maximum 850 μm intensity in Jy beam^{-1}. Column (6) lists the object "effective radius" in arcseconds, determined from the square root of the area of the object found by CLUMPFIND divided by π. (Note that this is *not* the FWHM of a given object.) Column (7) lists the median 850 μm noise in Jy beam^{-1} of all pixels associated with the object (defined by CLUMPFIND). Column (8) lists the signal-to-noise ratio of the detection, i.e., the ratio of the maximum 850 μm intensity (see col. [5]) to the median 850 μm noise (see col. [7]). Column (9) lists the object 850 μm flux in Jy, derived as the flux of the object over its area defined by CLUMPFIND (i.e., down to a level equal to 3 times the minimum noise of the map of origin). To determine 850 μm fluxes, a Gaussian beam of 22.9″ FWHM was assumed (see § 4).

Columns (10)–(14) provide other 850 μm characteristics for each object. Column (10) lists an alternative 850 μm flux in Jy,

derived as the flux within an alternative area, i.e., that defined by a contour of 3×30 mJy beam^{-1} = 90 mJy beam^{-1} for all possible objects. Determining fluxes for all objects within a common intensity threshold allows fluxes between objects to be compared more easily. The common threshold of 30 mJy beam^{-1} was chosen to be representative of typical noise levels of the 850 μm maps, as seen in Figure 8. Column (11) lists an effective radius of an alternative area for each object, i.e., where pixels had 850 μm intensities $\geq$90 mJy beam^{-1}. Column (12) is a flag for the 850 μm data. If the maximum 850 μm intensity (col. [5]) is $\geq 5 \times 30$ mJy beam^{-1} = 150 mJy beam^{-1}, column (12) is blank. Otherwise, column (12) lists "c" and columns (10) and (11) list the dummy values "−99.99" and "−99.9," respectively. Columns (13) and (14) list respectively the minimum and median noise values at 850 μm from the square degree map from which the object was identified (i.e., col. [4]).

Columns (15)–(19) list, if available, the 450 μm characteristics for each object. Again, CLUMPFIND was not used on the 450 μm maps to define objects; instead, 450 μm characteristics for each object are determined using the alternative area described above, i.e., the angular extent where their 850 μm intensities $\geq$90 mJy beam^{-1}. Column (15) lists the median 450 μm noise in Jy beam^{-1} over the alternative area of the object. If the maximum 450 μm intensity within the alternative area (col. [11]) is >3 times the median 450 μm noise, column (16) (a flag) is blank, column (17) lists the maximum 450 μm intensity in Jy beam^{-1}, column (18) (another flag) is blank, and column (19) lists the 450 μm flux of the object in Jy, assuming a Gaussian beam of 17.3″ FWHM (see § 4). Otherwise, columns (16) and (18) list "<", column (17) lists an upper limit equal to 3 times the median 450 μm noise, and column (19) lists a 450 μm flux upper limit determined by assuming each pixel within the alternative area (col. [11]) contains a value equal to 3 times the median 450 μm noise.

---

[8] To convert from J2000.0 to Galactic coordinates, the J2000.0 position of the North Galactic pole was assumed to be ($12^h51^m26.28^s$, $+27°07'41.7''$) and the Galactic longitude of the ascending node of the Galactic equator was assumed to be 32.93192°, following the ICRS system values of these provided in the Hipparcos Catalogue (ESA 1997).
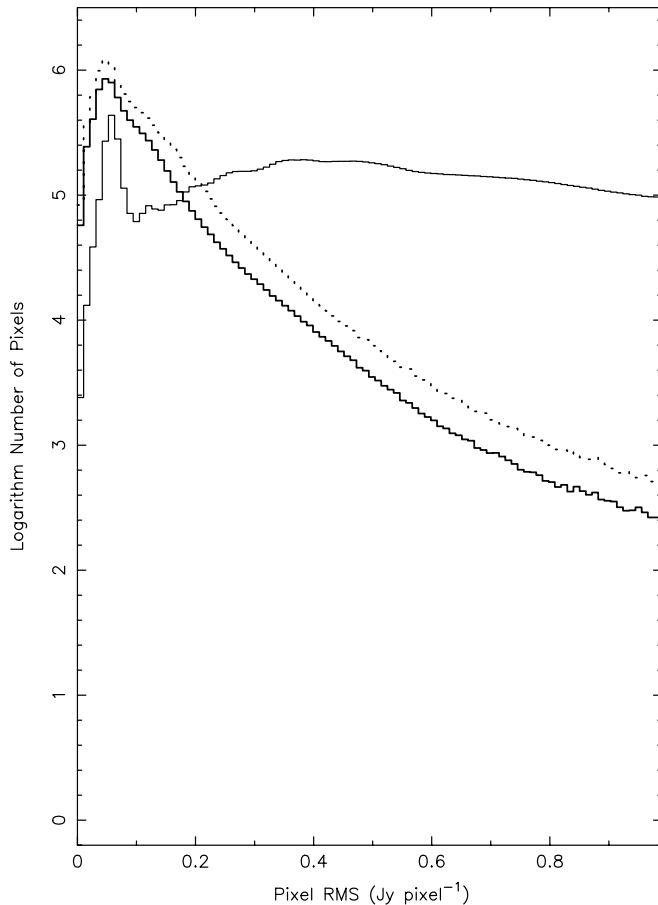
Fig. 8.— Histograms showing the distribution of $1\,\sigma$ rms per pixel from all pixels in the 850 μm Extended maps (*dotted heavy line*), 850 μm Fundamental maps (*solid heavy line*), and the 450 μm Fundamental maps (*solid thin line*). The distributions have been truncated at 1.0 Jy beam^{-1}.
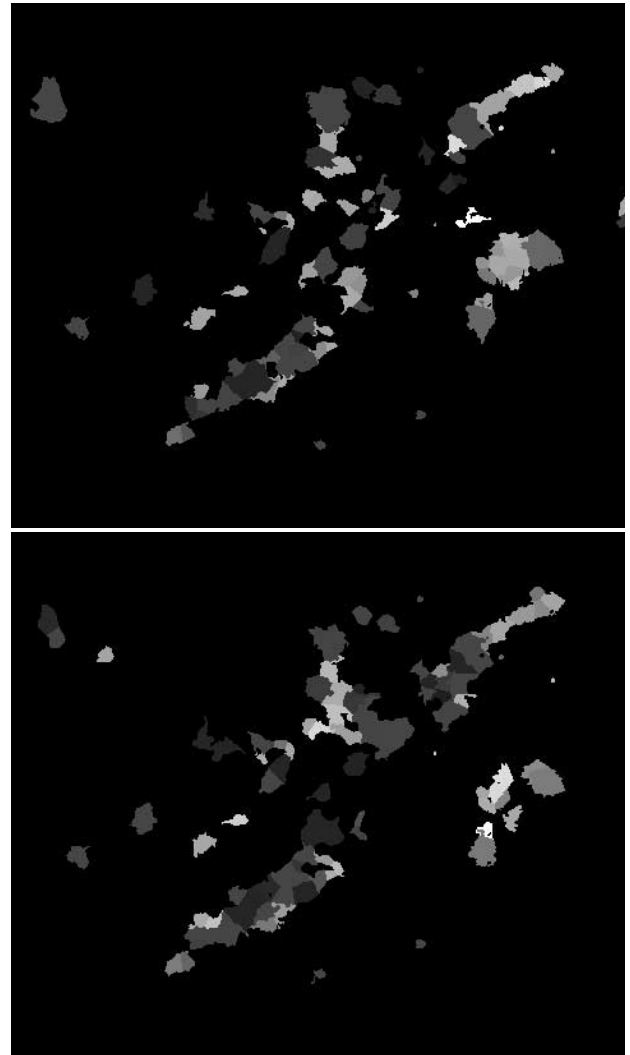

Fig. 9.— Differences in L1688 objects in the Fundamental (*top*) and Extended (*bottom*) Data Sets where different objects in each data set are shown by different shades of gray.

Columns (20)–(23) list, if available, the ratios of two wavelength data for each object. For these ratios, the 850 and 450 μm maps were convolved with beams from the other respective wavelength to produce maps at each wavelength with a common beam size. (After this convolution, both maps are at the same resolution and have common "error beams.") If an upper limit to the maximum 450 μm intensity is *not* given, column (20) (a flag) is blank, column (21) lists the ratio of maximum intensity at 450 to that at 850 μm for each object, column (22) (a flag) is blank, and column (23) lists the ratio of the flux at 450 μm to the flux at 850 μm for each object, determined over the alternative area described. If the maximum 450 μm intensity (col. [17]) is an upper limit, columns (20) and (22) list "<", and column (21) lists an upper limit to the intensity ratio where the maximum 450 μm intensity upper limit is equal to 3 times the median 450 μm noise, corrected to take into account the larger beam size of the convolved 450 μm map. Furthermore, column (23) lists in this case an upper limit to the flux ratio where the 450 μm flux upper limit is equal to that determined assuming each pixel in the convolved map within the alternative area contains a value equal to 3 times the beam-corrected median 450 μm noise. Note that the large uncertainties of the 850 and 450 μm fluxes make the uncertainties in their ratios accordingly large, i.e., >60%.

Column (24) provides further flags for the 450 μm data. If the actual median 450 μm noise (col. [15]) was >999 Jy beam^{-1}, column (24) lists "n". In addition, if no 450 μm data are present at the location of the object, column (24) lists "M". Finally, if the maximum 850 μm intensity of the object is not $\geq$150 mJy beam^{-1}, column (24) lists "c", in a manner similar to column (12). In all these cases, columns (15)–(19) list the dummy values "−99.99."

Column (25) indicates the proximity of the object to the edge of its respective mapped area. The maximum intensities and fluxes of an identified object can be considered accurate only if it has been sampled in its entirety across the sky. To provide a sense of this accuracy, column (19) lists either "clear" or "edge" for each object. If the former is the case, the object was defined without any pixel extending to an area of the sky not mapped by SCUBA. If the latter is the case, the object extends to a map edge, and the determined fluxes should be considered only as lower limits.

Column (26) lists potential identifications of the cataloged objects from other catalogs. These were obtained from the SIMBAD astronomical database using a bulk request for objects in the literature that were located within an 11.5″ radius (i.e., half the effective FWHM of the 850 μm beam) of the position of maximum brightness at 850 μm, as defined in column (1). The object chosen for column (26) was that which was closest to the position of maximum 850 μm intensity. Given that many astronomical objects have several names, we prioritized the identification of objects based on their name, or if not named, identification within the

TABLE 2

FUNDAMENTAL MAP OBJECT CATALOGUE

Object Identifier (1)	Galactic Longitude (deg) (2)	Galactic Latitude (deg) (3)	850 μm Maximum Intensity (Jy beam^{-1}) (5)	Object Size (arcsec) (6)	850 μm Median rms (Jy beam^{-1}) (7)	Peak S/N (8)	850 μm Flux (Jy) (9)	Alternative 850 μm Flux (Jy beam^{-1}) (10)	Alternative Object Flux (Jy beam^{-1}) (11)	850 μm lag (12)	850 μm Minimum Map rms (Jy beam^{-1}) (13)	850 μm Median Map rms (Jy beam^{-1}) (14)
JCMTSF_J000134.7+231250......	108.3034	−38.2374	0.06	18.2	0.02	3.0	0.08	−99.99	−99.9	c	0.006	0.019
JCMTSF_J000136.0+231308......	108.3111	−38.2338	0.08	16.6	0.02	4.0	0.07	−99.99	−99.9	c	0.006	0.019
JCMTSF_J000136.8+231056......	108.3035	−38.2701	0.27	10.7	0.02	16.2	0.06	0.05	6.8		0.006	0.019
JCMTSF_J000137.3+231332......	108.3193	−38.2286	0.08	14.3	0.02	4.0	0.05	−99.99	−99.9	c	0.006	0.019
JCMTSF_J000137.7+231232......	108.3160	−38.2451	0.06	30.7	0.02	3.8	0.17	−99.99	−99.9	c	0.006	0.019
JCMTSF_J000138.6+231050......	108.3115	−38.2734	0.11	8.3	0.02	6.2	0.02	0.01	3.4		0.006	0.019
JCMTSF_J000138.9+233102......	108.4172	−37.9472	0.55	12.7	0.07	7.9	0.18	0.16	9.6		0.006	0.019
JCMTSF_J000141.5+232944......	108.4227	−37.9706	0.04	12.2	0.01	5.0	0.03	−99.99	−99.9	c	0.006	0.019
JCMTSF_J000141.6+231044......	108.3251	−38.2778	0.23	10.7	0.02	10.0	0.04	0.02	4.8		0.006	0.019
JCMTSF_J000142.9+231138......	108.3360	−38.2645	0.06	28.9	0.02	3.3	0.14	−99.99	−99.9	c	0.006	0.019
JCMTSF_J000146.8+232914......	108.4451	−37.9836	0.73	10.1	0.01	70.0	0.14	0.12	7.6		0.006	0.019
JCMTSF_J000358.6+683507......	118.6019	6.1135	0.86	33.0	0.07	11.7	1.91	1.91	33.0		0.048	0.076
JCMTSF_J000522.7+671751......	118.4975	4.8232	0.36	39.8	0.08	4.4	1.24	1.05	33.5		0.023	0.040
JCMTSF_J000754.5+352220......	113.0128	−26.6597	0.06	8.3	0.01	4.3	0.02	−99.99	−99.9	c	0.008	0.021
JCMTSF_J000953.3+255525......	111.3672	−36.0133	0.06	12.2	0.01	5.0	0.04	−99.99	−99.9	c	0.011	0.019
JCMTSF_J000955.1+255356......	111.3693	−36.0389	0.69	11.2	0.09	7.3	0.17	0.15	8.3		0.011	0.019

NOTE.— Table 2 is published in its entirety (containing cols. [4] and [15]–[26], which includes the names of the source map of each entry and the 450 μm data) in the electronic edition of the *Supplement*. A portion is shown here for guidance regarding its form and content.

TABLE 3
EXTENDED MAP OBJECT CATALOGUE

Object Identifier (1)	Galactic Longitude (deg) (2)	Galactic Latitude (deg) (3)	850 μm Maximum Intensity (Jy beam^{-1}) (5)	Object Size (arcsec) (6)	850 μm Median rms (Jy beam^{-1}) (7)	Peak S/N (8)	850 μm Flux (Jy) (9)	Alternative 850 μm Flux (Jy beam^{-1}) (10)	Alternative Object Size (arcsec) (11)	850 μm Flag (12)	850 μm Minimum Map rms (Jy beam^{-1}) (13)	850 μm Median Map rms (Jy beam^{-1}) (14)
JCMTSE_J000134.7+231250	108.3034	−38.2374	0.06	18.2	0.02	3.0	0.08	−99.99	−99.9	c	0.006	0.019
JCMTSE_J000136.0+231308	108.3111	−38.2338	0.06	16.6	0.02	3.0	0.07	−99.99	−99.9	c	0.006	0.019
JCMTSE_J000136.8+231056	108.3035	−38.2701	0.27	10.7	0.02	16.2	0.06	0.05	6.8		0.006	0.019
JCMTSE_J000137.3+231332	108.3193	−38.2286	0.08	14.3	0.02	4.0	0.05	−99.99	−99.9	c	0.006	0.019
JCMTSE_J000137.7+231232	108.3160	−38.2451	0.06	30.7	0.02	3.8	0.17	−99.99	−99.9	c	0.006	0.019
JCMTSE_J000138.6+231050	108.3115	−38.2734	0.11	8.3	0.02	6.2	0.02	0.01	3.4		0.006	0.019
JCMTSE_J000138.9+233102	108.4172	−37.9472	0.55	12.7	0.07	7.9	0.18	0.16	9.6		0.006	0.019
JCMTSE_J000141.5+232944	108.4227	−37.9706	0.04	12.2	0.01	5.0	0.03	−99.99	−99.9	c	0.006	0.019
JCMTSE_J000141.6+231044	108.3251	−38.2778	0.23	10.7	0.02	10.0	0.04	0.02	4.8		0.006	0.019
JCMTSE_J000142.9+231138	108.3360	−38.2645	0.06	28.3	0.02	3.3	0.13	−99.99	−99.9	c	0.006	0.019
JCMTSE_J000146.8+232914	108.4451	−37.9836	0.73	10.7	0.01	58.3	0.16	0.14	8.3		0.006	0.019
JCMTSE_J000358.6+683507	118.6019	6.1135	0.82	42.1	0.06	14.4	3.16	3.16	42.1		0.055	0.078
JCMTSE_J000401.6+683901	118.6184	6.1765	0.27	30.8	0.06	4.5	1.03	1.03	30.8		0.055	0.078
JCMTSE_J000402.9+683619	118.6120	6.1319	0.48	46.4	0.06	7.9	3.14	3.14	46.4		0.055	0.078
JCMTSE_J000411.6+683837	118.6322	6.1672	0.46	41.6	0.06	7.6	2.24	2.24	41.6		0.055	0.078
JCMTSE_J000413.9+683619	118.6286	6.1289	0.44	52.2	0.06	7.2	4.34	4.34	52.2		0.055	0.078

NOTE.— Table 3 is published in its entirety (containing cols. [4] and [15]–[26], which includes the names of the source map of each entry and the 450 μm data) in the electronic edition of the *Supplement*. A portion is shown here for guidance regarding its form and content.
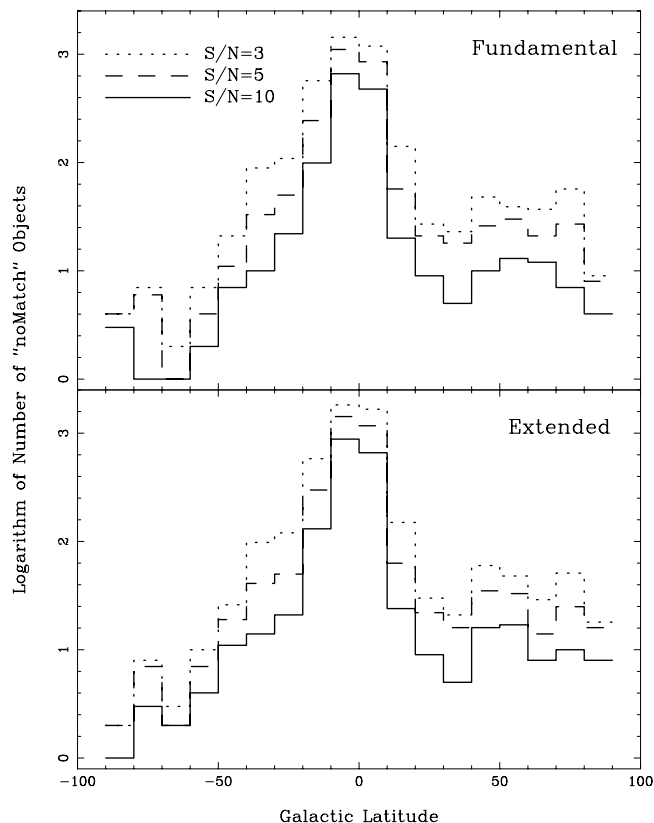
Fig. 10.—Logarithmic histograms of the numbers of unidentified objects with Galactic latitude in the FMOC (*top*) and the EMOC (*bottom*). Such objects are those labeled "noMatch" in col. (26) of Tables 2 and 3.

NGC, IC, 3C, HD, SAO, BD, or IRAS catalogs. (In cases of identification in several of these catalogs, the entry in col. [26] was decided in order of how these catalogs were just listed.) Many objects, however, are not found within these specific catalogs but were identified in various other studies. Following the nomenclature of the SIMBAD database, we include in column (26) the bibliographic abbreviation of these studies, along with the identification in that study. If the SIMBAD database did not contain an identified object within an 11.5″ radius, column (26) lists instead "noMatch". Note that extended objects can have very poorly defined positions (e.g., dark nebulae with positions determined from extinction maps), and in some cases these have been listed as "noMatch" when its SIMBAD position is separated from the SCUBA 850 μm position by >11.5″. For interest, Figure 10 shows histograms of the numbers of objects above signal-to-noise ratio thresholds of 3, 5, and 10 (see col. [8]) with Galactic latitude (see col. [3]) that are listed as "noMatch" in column (26) in the FMOC and EMOC. At $|b| > 30$, there are 343, 189, and 75 unidentified objects seen in the FMOC and 374, 217, and 99 such objects are seen in the EMOC at signal-to-noise ratios ≥3, 5, and 10, respectively (see § 7.1 for further discussion of object identification).

In the FMOC, the object with the largest maximum 850 μm intensity seen by SCUBA was the "Large Molecular Heimat," associated with Sgr B2 with 242.68 Jy beam^{-1}. In addition, the object with the largest 850 μm flux seen by SCUBA was "SMA 1," associated with the Orion BN/KL region at 599.6 Jy. The total 850 μm flux of all objects identified in the FMOC is 20,868.08 Jy.

Figure 11 shows histograms of the number of sources as a function of size (arcseconds), maximum 850 μm intensity (Jy beam^{-1}), and total 850 μm flux (Jy) for objects from the FMOC given a common sensitivity threshold (i.e., size determined at the

90 mJy beam^{-1} level; see Table 2, cols. [10] and [11]). The top left panel of Figure 11 shows that a majority of the sources have sizes (as measured by CLUMPFIND) that are resolved, with a peak in the distribution at ∼30″. The top right panel of Figure 11 shows the maximum 850 μm intensities. These rise steeply toward small values and have a turnover at ∼0.2 Jy beam^{-1}, likely due to the intrinsic sensitivities of the maps. The bottom left panel of Figure 11 shows the total 850 μm fluxes with a peak near 2 Jy. This distribution likely suffers from incompleteness at smaller fluxes, since CLUMPFIND searches out to only a fixed intensity limit and thus underestimates the true flux of sources with low peak values and extents. The bottom right panel of Figure 11 plots the cumulative flux for all sources. The integrated flux rises rapidly with lower total flux sources until reaching the point where the histogram turns over. In both the FMOC and EMOC the mean 850 μm flux per source is ∼4 Jy, while the median 850 μm flux is ∼1 Jy.

7. ROBUSTNESS OF THE CATALOGUES

In this section, we demonstrate the robustness of the catalogues by comparing examples of catalogue entries to various published data. In addition, we show by example several caveats that must be considered when interpreting data from the SCUBA Legacy Catalogues.

7.1. *Object Identification*

Our object identification strategy does a good job of identifying locations of emission in each image. For example, Johnstone et al. (2001) found that most of the 67 objects identified by CLUMPFIND in 850 μm maps of Orion B were largely the same as those identified subjectively (by eye) in the same maps by Mitchell et al. (2001), with differences seen for only a few very faint objects. Figure 12 shows the number of objects of signal-to-noise ratio greater than or equal to a nominal signal-to-noise ratio in each catalogue. The number of objects in each catalogue with signal-to-noise ratios ≥3 is of course equal to the number of objects in each respective catalogue, and these numbers drop dramatically with ever higher thresholds. We have chosen the minimum local signal-to-noise ratio as 3 for each catalogue, since this level allows the inclusion of emission that appears subjectively real (by eye) in their parent maps. Although this minimum signal-to-noise ratio is arguably low, recall that the objects were identified not as single pixels above this level, but were identified from closed positive contours enclosing an area at least as large as the beam. Note, however, that the catalogues can be easily altered to include only objects above certain levels of signal-to-noise ratio by using column (8) of Tables 2 or 3 as a filter.

Despite its effectiveness, our object identification strategy is not perfect. *Any judgment about a given object in the catalogues, regardless of its respective signal-to-noise ratio, should not be made without first examining carefully its parent map.* Although we have attempted to remove artifacts by imposing size, signal-to-noise ratio, and edge-proximity criteria to all objects, artifacts may still remain in some maps. The inherent heterogeneity of the SCUBA data means that applying uniform criteria is difficult. Regardless of whatever practical criteria are applied, some artifacts will be misidentified as objects, and some real emission will be not identified as objects.

To illustrate our object identification strategy and demonstrate its limits, we provide three examples of maps from the Fundamental Map Data Set. Figures 13–15 show 850 μm maps of L1551, M51, and NGC 7538, respectively, with contours that delineate the boundaries of objects identified in each image by the
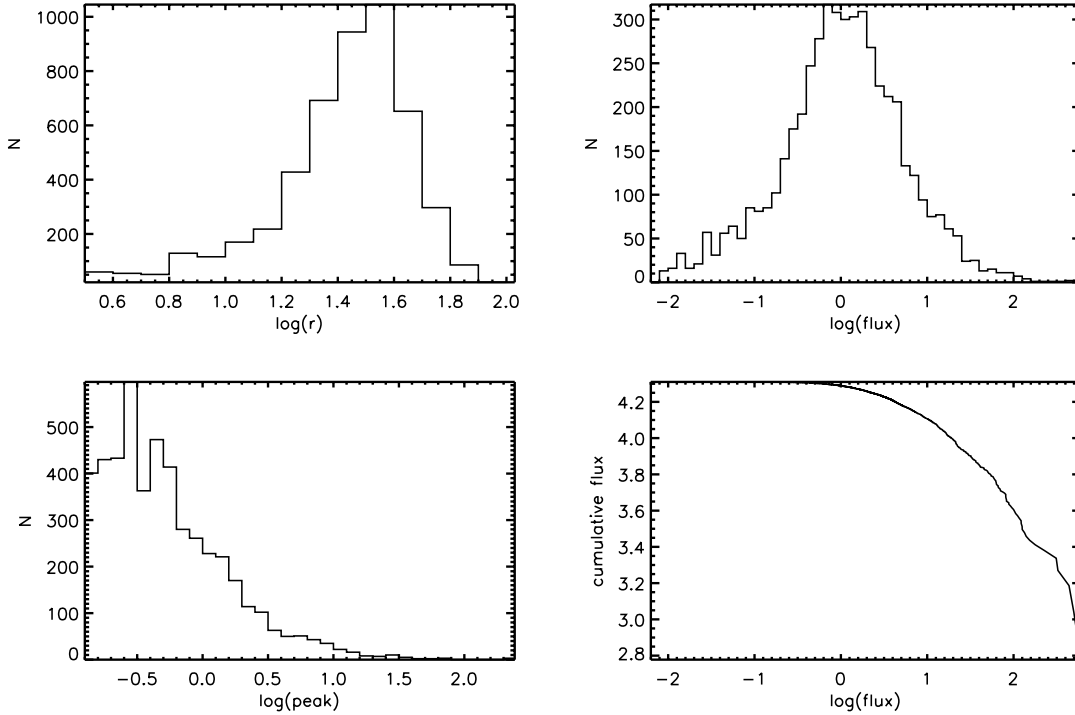
Fig. 11.—Summary plots of the FMOC. *Top left*: Histogram of the logarithmic distribution of the alternative effective sizes in arcseconds of all objects down to the 90 mJy beam^{-1} contour (col. [11] of Table 2). *Top right*: Histogram of the logarithmic distribution of the alternative 850 μm fluxes in Jy of these objects (col. [10] of Table 2). *Bottom left*: Histogram of the logarithmic distribution of maximum 850 μm intensities in Jy beam^{-1} of these objects (col. [5] of Table 2). *Bottom right*: Cumulative logarithmic distribution of the alternative 850μm flux in Jy of these objects.

CLUMPFIND algorithm that have passed our criteria. Each example map shows emission that can be associated with actual astronomical objects. In Figures 13 and 14 we see examples of low surface brightness emission that has been divided into multiple objects and weak objects that may be misidentified image artifacts. In Figures 14 and 15 we see examples of emission that remained unidentified as objects due to criteria imposed on each map.

In the 850 μm map of L1551 (Fig. 13), 22 objects are identified. The three brightest are L1551 IRS 5, HL Tau, and L1551-NE, located at the image center. These have signal-to-noise ratios >70 and were easily identified by CLUMPFIND. Another source is seen 2′ directly south of HL Tau with a signal-to-noise ratio of 6. This source corresponds to HH 30 and is seen because the local rms level is unusually low (5 mJy beam^{-1}) in the ~2′ diameter region around HL Tau, as this region was observed repeatedly as a calibrator throughout SCUBA's lifetime (see Moriarty-Schieven et al. 2006). About 5′ northeast of L1551-NE and ~2′−5′ west of IRS 5, nine objects were identified with signal-to-noise ratios of 3−11, real features that are likely associated with dust compressed by the strong outflows from L1551-NE or IRS 5. Given the relatively lower surface brightness of these features and thus the greater influence of noise on their structure, CLUMPFIND has divided them into multiple objects. A similar division into three objects is found toward the diffuse, lower surface brightness feature known as L1551-MC (see Swift et al. 2005) located ~7′ northwest of IRS 5. Toward the map edges, i.e., ~10′ southwest and ~10′ east of IRS 5, three objects were identified, all with low signal-to-noise ratios of 3−4. Given the proximity of these to the map edge and to obvious bright artifacts at the edge (induced by imperfect image flattening), these objects are likely themselves artifacts. Since it is difficult to know from the map alone that these latter objects are *not* artifacts, however, we retain such features as

objects, leaving their inclusion or exclusion for further analysis up to individuals.

In the 850 μm maps of M51 (Fig. 14), five objects are identified. The brightest two, each with signal-to-noise ratios of ~13, are located at the galaxy nucleus in the center of the map. The next brightest object, with a signal-to-noise ratio of ~6, is located 5′ north-northeast of the M51 nucleus and is associated with the nucleus of NGC 5195. A fourth object, with a signal-to-noise ratio of ~5, is associated with a bright clump to the southwest of the M51 nucleus along a spiral arm near the position of the H II region CCM 72. Although faint emission from the spiral arms of M51 is clearly seen in the image, no other locations in the arms were bright enough relative to the local noise in this image to have been identified as objects. The fifth "object" in Figure 13 with a signal-to-noise ratio of ~4, however, consists of a large low surface brightness feature that is likely an artifact of imperfect flattening in the image, similar to those seen near the edges of the L1551 map. (Note the extreme high and low amplitudes seen at the map edges to the east and west, respectively; a custom background subtraction to remove the edge problems and improve the detection of extended emission from M51 itself, was done by Meijerink et al. [2005].)

In the 850 μm maps of NGC 7538 (Fig. 15), 17 objects are identified. In comparison, Reid & Wilson (2005) located 77 objects in their 850 μm map of this region, because this map had smaller pixels (2″) and a smaller beam (15.3″ FWHM). In addition, they constructed their map using a different technique ("Emerson2" reconstruction). (Of the three examples discussed here, only this region had objects identified within using CLUMPFIND by other authors.) All objects in Figure 14 are composed of several objects identified by Reid & Wilson. The brightest three, located at the map center, correspond to IRS 1-3, IRS 11, and IRS 9 (respectively,
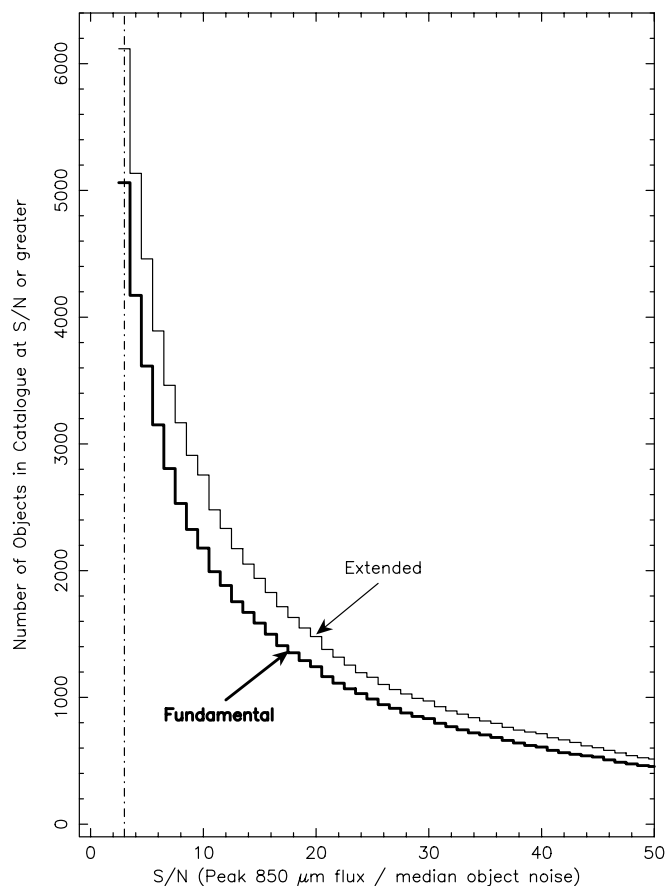
FIG. 12.—Histogram of the numbers of objects in either the Fundamental or Extended Map Object Catalogues at a given signal-to-noise ratio level or above.

FIG. 13.—850 μm map of the LDN 1551 cloud from the Fundamental Data Set. Intensities at 850 μm range from -0.1 to 0.42 Jy beam^{-1} (*gray scale*). Squares denote positions of maximum intensity for each object in this map listed in the Fundamental Map Object Catalogue (Table 2); these positions correspond to the identifiers of each object (col. [1] of Table 2). The labels denote the maximum signal-to-noise ratio of each object (col. [8] of Table 2). Dark contours delineate the outer boundaries of each object.

SMM 46, SMM 48, and SMM 60 of Reid & Wilson), and have signal-to-noise ratios of >70. The next brightest object, located $\sim2'$ northwest of IRS 1-3 and with a signal-to-noise ratio of ~35, is adjacent to IRS 4. Twelve of the remaining 13 objects have signal-to-noise ratios of $\sim7-23$ and each appears associated with real emission. The last object, $\sim2'$ southeast of IRS 9 and with a signal-to-noise ratio of 3, also arguably appears associated with real emission; for example, Reid & Wilson identified this emission with their objects SMM 69, SMM 70, and SMM 71. Unlike the previous two maps, no objects are identified toward the map edges that may be artifacts. Notably, the map contains much weaker large-amplitude artifacts near the edge than noted in the previous two maps. Conversely, however, emission that is likely real has been not identified as an object given its proximity to the map edge, i.e., the emission seen $\sim6'$ west of IRS 1 that is associated with SMMs 1–7 of Reid & Wilson.

Regarding the completeness of the CLUMPFIND algorithm, we stress that object candidates in various maps were identified down to very low noise levels in each map, and then we used other criteria (maximum intensity vs. local median noise, relative location within maps) to preclude candidates from the object catalogues. We have not attempted, however, to quantify the completeness of the CLUMPFIND algorithm, e.g., by inserting artificial sources into the maps to determine how well CLUMPFIND recovers such sources. The objects identified in the catalogues encompass a large variation of size and morphology, and the maps themselves can have large differences in noise both within themselves and between maps. Such variety makes it difficult to make definitive tests for completeness across all maps. For reference, however, we note that Enoch et al. (2006) performed empirical tests for
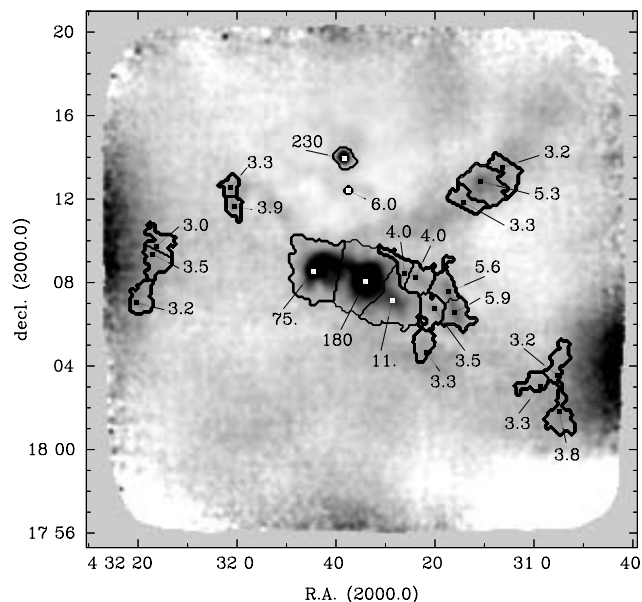
completeness using Monte Carlo simulations of the identification of artificial Gaussian sources of various size in empty regions of their wide-field 1.3 mm continuum map of the Perseus cloud, which had a reasonably small noise level across the map ($\sim15\%$). Such tests defined completeness limits in mass and size, and the ~100 actual objects they identified by CLUMPFIND in their maps study were bounded on the mass-size plane by an empirically
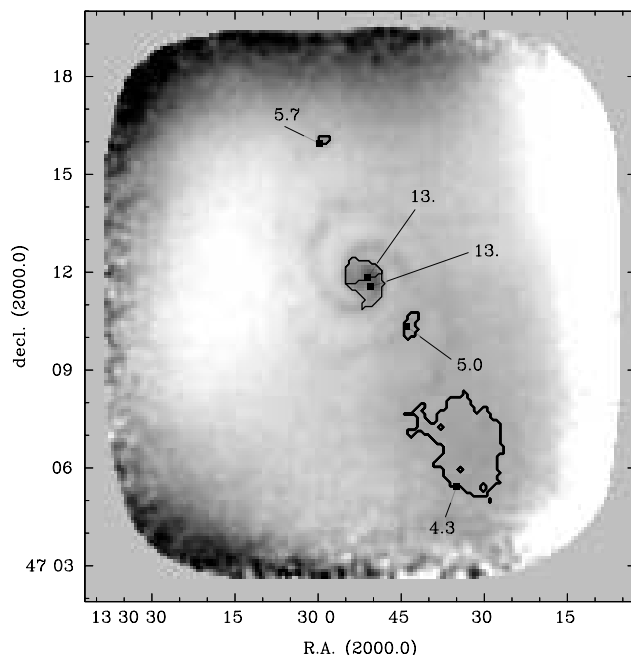

FIG. 14.—850 μm map of the galaxy M 51 from the Fundamental Data Set. Intensities at 850 μm range from -0.1 to 0.32 Jy beam^{-1} (*gray scale*). Symbols, labels, and contours are defined as in Fig. 13.
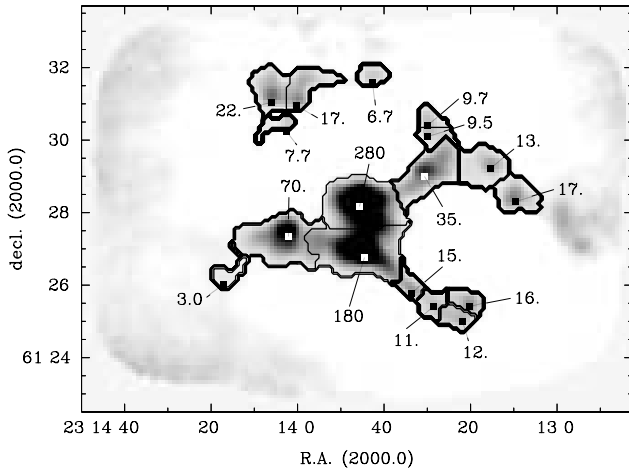
Fig. 15.—850 μm map of the NGC 7538 massive star-forming region from the Fundamental Data Set. Intensities at 850 μm range from -0.1 to 3.2 Jy beam^{-1} (*gray scale*). Symbols, labels, and contours are defined as in Fig. 13.

determined 10% completeness limit, i.e., the level where 10% of their artificial sources were recovered.

In summary, we believe our object identification algorithm does an effective job of locating real emission within the 850 μm maps, but it cannot be considered perfect. The reality of any given object as an astronomical source in the Fundamental or Extended Catalogues must be considered carefully by those interested in these data.

7.2. *Flux Comparison*

As described earlier in § 3, flux calibration was performed on the SCUBA maps using the most recent flux conversion factors available in the JCMT archive. In addition, we modified slightly the flux scale of all maps to bring the intensities of the point-source calibrators HL Tau, CRL 618, and CRL 2688 in line with those reported on the JCMT Web site (see Table 1). In this section, we compare intensities obtained from our reprocessed maps with those from published maps that were processed by others. In particular, we compare the maximum intensities of objects in the Fundamental Catalogue with those found in published maps after smoothing by a Gaussian of $\sigma = 6''$, binning to $6''$ pixels, and regridding to the same pixel positions as in our maps using various tasks in the MIRIAD software package (Sault et al. 1995).

Following the discussion above, we compared our Fundamental Data Set 850 μm maps of L1551 and NGC 7538 to published data of the same, kindly provided by G. Schieven and M. Reid, respectively. From each region, a total of 10 or 14 objects, respectively, were chosen by eye from the smoothed, rebinned, and regridded maps, and the maximum intensities were measured. Figure 16 shows the comparison between our maximum intensities and those from the published data at 0–3 Jy beam^{-1}. For L1551 and NGC 7538, the median percent differences between maximum intensities of objects in the published data and their counterparts in the Fundamental Catalogue are 16.2% and -12.8%, i.e., within the 20% uncertainties expected for 850 μm SCUBA data (see § 3). The smallest maximum intensity differences (<2%) are found for the brightest objects in both regions (>3 Jy beam^{-1}; not shown in Fig. 16).

Beyond different flux calibration approaches, a major component of the difference between the intensities in these maps is likely the difference between how large-scale flux variations are
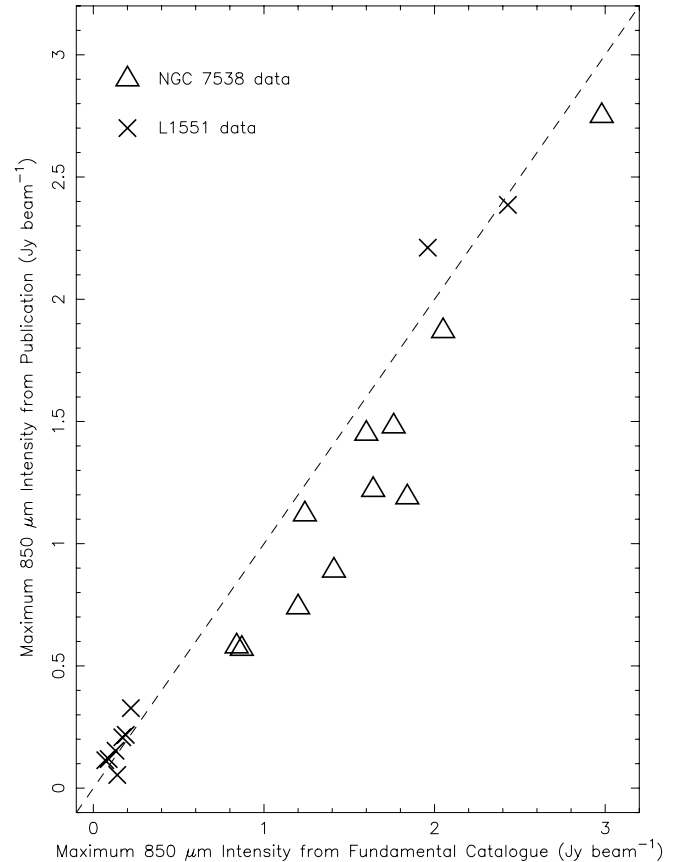

Fig. 16.—Comparison of maximum 850 μm intensities in LDN 1551 (*crosses*) and NGC 7538 (*triangles*) between objects in the Fundamental Data Set maps and those in smoothed and rebinned maps by Moriarty-Schieven et al. (2006) and Reid & Wilson (2005), respectively. The dashed line denotes the line of equality.

removed by different authors. As described in § 3, the Legacy Catalogue maps have been "flattened" by subtracting a very smoothed map from the original map, but different authors have different approaches to the problem of establishing a "zero point" to SCUBA maps. Note, however, that our technique explicitly excluded brighter sources from smoothing prior to flattening, which may account for the smaller differences in intensities between maps for these sources described above.

To compare the fluxes between objects, the published and Fundamental Data Set maps were clipped according to the extents of the objects defined in the Fundamental Catalogues. The percent differences in total fluxes at 850 μm for L1551 and NGC 7538 between the former and latter maps were 24% and -29%, respectively. Accordingly, the absolute uncertainties of fluxes at 850 μm of objects in the FMOC may be as large as ±30%. Correspondingly, the absolute uncertainties of fluxes at 450 μm of objects in the FMOC may be as large as ±100%, since sky subtraction and flattening are even more difficult at that wavelength.

7.3. *Pointing Differences*

Pointing corrections for SCUBA were determined from short observations of bright, pointlike calibrators. Given variations in weather and dish surface conditions over the 9 years SCUBA was in operation, it is thus difficult to assign a specific pointing uncertainty to the entire SCUBA data set. Moreover, different observers may have used different schemes over time. For example, note the $\sim6''$ offset evident in our map of NGC 1333 relative to those made by Sandell & Knee (2001) from early SCUBA data.
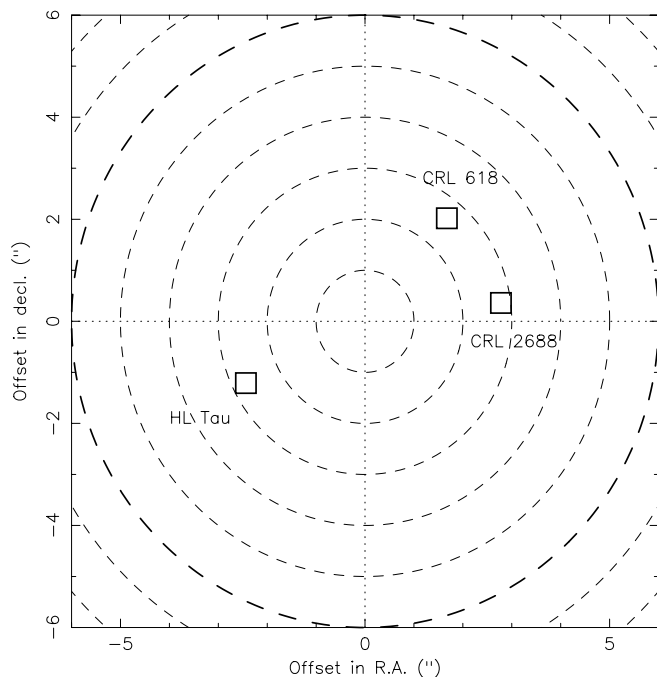
Fig. 17.—Relative offsets between expected positions of the pointlike calibrators HL Tau, CRL 618, and CRL 2688 (at center) and the positions of the pixel of maximum 850 μm intensity for the corresponding object in Fundamental Map Object Catalogue (*squares*). The dashed circles denote angular offsets starting at 1″ radius and increasing in steps of 1″ radius. The heavy dashed circle denotes an angular offset of 6″, equal to 1 σ of the narrow component of the *unsmoothed* JCMT beam at 850 μm.

To determine a pointing uncertainty, we compare the J2000.0 positions of the three pointlike calibrators, HL Tau, CRL 618 (PN G166.4−06.5), and CRL 2688 (the Egg Nebula) as provided by SIMBAD to the J2000.0 position of the pixel of maximum intensity at 850 μm for each respective source from our data sets. Not only are these particular objects compact with well-defined maxima, they also have bright optical counterparts with fairly well-established positions. (Note that relatively few objects detected at submillimeter wavelengths have optical counterparts and, correspondingly, have relatively poorly determined positions.) Figure 17 shows the difference between the expected positions at (0, 0) and the location of the pixel of maximum intensities. Note that there is no consistent directional offset between the expected positions and positions of maximum intensity. The mean magnitude of the angular offset between these positions is 2.7″, or less than half the 6″ pixel size of the 850 μm maps in the data sets and ∼14% of the 19.5″ FWHM of the narrow Gaussian component of the 850 μm beam (see Fig. 7). (Note that 6″ is also equal to 1 σ of the Gaussian representing the narrow component of the *unsmoothed* JCMT beam at 850 μm; see the heavy dashed circle in Fig. 17.) Furthermore, the angular offsets shown in Figure 17 are only to the positions of the respective pixel of maximum intensity, which were used to identify objects in the catalogues. Gaussian fits to the 850 μm emission of each pointlike source (where Gaussians are particularly effective) yield even closer positional coincidence. For example, a mean angular offset magnitude of only 0.93″ is found between the expected positions and those of the peaks of the Gaussian fits to these particular objects.

7.4. *Associations with Known Objects*

Column (26) in both catalogues (Tables 2 and 3) lists tentative associations of each object with those found in the SIMBAD astro-nomical database (i.e., known objects located <11.5″ from the position of maximum 850 μm intensity.) Given the low resolution of the data set maps relative to optical or infrared observations, which compose the bulk of the SIMBAD entries, we stress that these associations are tentative. For the Fundamental Catalogue, our original search through SIMBAD of 7031 object candidates[9] resulted in potential associations with 7882 SIMBAD objects; sometimes many SIMBAD objects were found within 11.5″ of the FMOC position. To differentiate between multiple potential associations, we chose objects in SIMBAD that were closest to the position of maximum 850 μm intensity. Of these objects, an identifier in column (26) was chosen based on a either a name or entry within eight catalogs (NGC, IC, 3C, HD, SAO, BD, or IRAS in descending order of priority.) Out of the 7031 objects, only 1592 had associations with SIMBAD objects.

To test for false associations, all 7031 positions in the early FMOC were shifted north or south by 5′, and these new positions were run through SIMBAD. These new positions resulted in only 430 or 383 potential SIMBAD associations, respectively, much less than the 7882 found earlier. In addition, out of the 7031 positions shifted north or south, only 356 or 322, respectively, had associations with SIMBAD objects, again, much less than the 1592 found earlier. From these numbers, we surmise that the probability for false association in the catalogues is relatively low, only ∼20% (340/1600). We note, however, that the SIMBAD database is not itself an all-sky survey, but rather a collection of known objects. What is listed in column (26) only indicates tentative association with previously found objects.

8. DATA PRODUCTS

The 850 and 450 μm square degree maps from the Fundamental Data Set and the 850 μm maps from the Extended Data Set are available for download from the SCUBA Legacy Catalogues repository at the CADC.[10]

Each emission map is in the standard FITS format projected onto the tangent plane from its center position. Each map file is named by the Galactic coordinates of its center position. For example, the FITS file `scuba_F_178d6_-19d8_850um.emi.fits` contains the square degree SCUBA 850 μm emission map from the Fundamental Data Set (F) centered at $(l, b) = (178.6, -19.8)$. (This particular map contains a nice 850 μm image of L1551; see Figs. 3c and 13.) Note that files of maps from the Extended Data Set are identified with an "E" instead of an "F."

In addition to the emission maps, the repository contains other useful files, including the error map and coverage map corresponding to each 850 μm emission map. These files are named as above but the names end in `850um.err.fits` or `850um.cov.fits`, respectively, instead, e.g., `scuba_F_178d6_-19d8_850um.err.fits` or `scuba_F_178d6_-19d8_850um.cov.fits`. The repository also contains the error map corresponding to each 450 μm emission map.

The repository contains additional information about the objects identified in the 850 μm maps of the Fundamental or Extended Data Sets. For example, it has ASCII text files containing the FMOC and EMOC, e.g., `scuba_FMOC.txt` and `scuba_EMOC.txt`, respectively. Finally, the repository contains object maps where the pixels give the numerical identifications made by CLUMPFIND for each object in respective 850 μm

---

[9] SIMBAD source association was performed prior to some final culling of object candidates. Hence the number of objects that was examined for the Fundamental Data Set was 7031 rather than the final 5061.

[10] Available online at http://www.cadc.hia.nrc.gc.ca/community/scubalegacy.

emission maps. No such map was produced if no objects were found in the respective emission map. These files are named as above, but the names end in `850um.obj.fits` instead, e.g., `scuba_F_178d6_-19d8_850um.obj.fits`.

9. CONCLUSIONS

In this paper, we described the bulk processing of SCUBA map data in the JCMT public archive, done to provide a resource of reduced 850 and 450 μm continuum data for the community and to aid future work at submillimeter and millimeter wavelengths. The maps are composed of a Fundamental Map Data Set at 850 and 450 μm and an Extended Map Data Set at only 850 μm. In the former data set, only data with superior atmospheric correction data were included, and in the latter, almost all available data were included. Because of the specific way in which their data were collected, we do not include single chop data from deep surveys for high-redshift galaxies, since the matrix inversion process did not generate satisfactory maps. In addition, we described two catalogs of objects identified in the Fundamental Map and Extended Map Data Sets, each determined using the automated CLUMPFIND identification algorithm. Maps of 850 and 450 μm

emission as well as respective error, coverage, and object identification maps, and the catalogs, will be available for download from the CADC.[11]

[11] Available online at http://www1.cadc-ccda.hia-iha.nrc-cnrc.gc.ca/jcmt/.

REFERENCES

Archibald, E. N., Dunlop, J. S., Jimenez, R., Friaça, A. C. S., McLure, R. J., & Hughes, D. H. 2002, MNRAS, 336, 353

Beichman, C. A., Helou, G., & Walker, D. W. 1988, Infrared Astronomical Satellite (IRAS): Catalogues and Atlases, Vol. 1, Explanatory Supplement (NASA RP-1190; Washington: GPO)

Coppin, K., et al. 2006, MNRAS, 372, 1621

Economou, F., Bridger, A., Wright, G. S., Jenness, T., Currie, M. J., & Adamson, A. 1999, in ASP Conf. Ser. 172, Astronomical Data Analysis Software and Systems VIII, ed. D. M. Mehringer, R. L. Plante, & D. A. Roberts (San Francisco: ASP), 11

Emerson, D. T. 1995, in ASP Conf. Ser. 75, Multi-Feed Systems for Radio Telescopes, ed. D. T. Emerson & J. M. Payne (San Francisco: ASP), 309

Emerson, D. T., Klein, U., & Haslam, C. G. T. 1979, A&A, 76, 92

Enoch, M., et al. 2006, ApJ, 638, 293

Gezari, D. Y., Schmitz, M., & Mead, J. M. 1984, Catalog of Infrared Observations (NASA RP-1118; Washington: GPO)

———. 1988, Far Infrared Supplement: Catalog of Infrared Observations (2nd ed., NASA RP-1205; Washington: GPO)

ESA. 1997, The Hipparcos and Tycho Catalogues (ESA SP-1200; Noordwijk: ESA)

Hogerheijde, M. R., & Sandell, G. 2000, ApJ, 534, 880

Holland, W. S., et al. 1999, MNRAS, 303, 659

———. 2006, Proc. SPIE, 6275, 45

Jenness, T., Stevens, J. A., Archibald, E. N., Economou, F., Jessop, N. E., & Robson, E. I. 2002, MNRAS, 336, 14

Johnstone, D., & Bally, J. 2006, ApJ, 653, 383

Johnstone, D., Di Francesco, J., & Kirk, H. M. 2004, ApJ, 611, L45

Johnstone, D., Fich, M., Mitchell, G. F., & Moriarty-Schieven, G. 2001, ApJ, 559, 307

Johnstone, D., Matthews, H., & Mitchell, G. F. 2006, ApJ, 639, 259

Johnstone, D., Wilson, C. D., Moriarty-Schieven, G., Giannakopoulou-Creighton, J., & Gregersen, E. 2000a, ApJS, 131, 505

Johnstone, D., Wilson, C. D., Moriarty-Schieven, G., Joncas, G., Smith, G., Gregersen, E., & Fich, M. 2000b, ApJ, 545, 327

Kirk, H. M., Johnstone, D., & Di Francesco, J. 2006, ApJ, 646, 1009

Knudsen, K. K., et al. 2006, MNRAS, 368, 487

Matthews, H. E. 1993, The James Clerk Maxwell Telescope: A Guide for the Prospective User (Hilo: JAC)

Meijerink, R., Tilanus, R. P. J., Dullemond, C. P., Israel, F. P., & van der Werf, P. P. 2005, A&A, 430, 427

Mitchell, G., Johnstone, D., Moriarty-Schieven, G., Fich, M., & Tothill, N. F. H. 2001, ApJ, 556, 215

Moriarty-Schieven, G. H., Johnstone, D., Bally, J., & Jenness, T. 2006, ApJ, 645, 357

Motte, F., André, P., & Neri, R. 1998, A&A, 336, 150

Reid, M. A., & Wilson, C. D. 2005, ApJ, 625, 891

Sandell, G., & Knee, L. B. G. 2001, ApJ, 546, L49

Sault, R. J., Teuben, P. J., & Wright, M. C. H. 1995, in ASP Conf. Ser. 77, Astronomical Data Analysis Software and Systems IV, ed. R. A. Shaw, H. E. Payne & J. J. E. Hayes (San Francisco: ASP), 433

Swift, J. J., Welch, W. J., & Di Francesco, J. 2005, ApJ, 620, 823

Weferling, B. 2005, MNRAS, 362, 263

Williams, J. P., de Geus, E. J., & Blitz, L. 1994, ApJ, 428, 693

Young, K. E., et al. 2006, ApJ, 644, 326